

The troublesome kernel

On hallucinations, no free lunches and the accuracy-stability trade-off in inverse problems*

Nina M. Gottschling[†] Vegard Antun[‡] Anders C. Hansen[§] Ben Adcock[¶]

December 21, 2024

Abstract

Methods inspired by Artificial Intelligence (AI) are starting to fundamentally change computational science and engineering through breakthrough performances on challenging problems. However, reliability and trustworthiness of such techniques is becoming a major concern. In inverse problems in imaging, the focus of this paper, there is increasing empirical evidence that methods may suffer from hallucinations, i.e., false, but realistic-looking artifacts; instability, i.e., sensitivity to perturbations in the data; and unpredictable generalization, i.e., excellent performance on some images, but significant deterioration on others. This paper presents a theoretical foundation for these phenomena. We give a mathematical framework describing how and when such effects arise in arbitrary reconstruction methods, not just AI-inspired techniques. Several of our results take the form of ‘no free lunch’ theorems. Specifically, we show that (i) methods that overperform on a single image can wrongly transfer details from one image to another, creating a hallucination, (ii) methods that overperform on two or more images can hallucinate or be unstable, (iii) optimizing the accuracy-stability trade-off is generally difficult, (iv) hallucinations and instabilities, if they occur, are not rare events, and may be encouraged by standard training, (v) it may be impossible to construct optimal reconstruction maps for certain problems, (vi) standard methods to improve reliability (e.g., regularization or adversarial training) may themselves lead to unstable problems. Our results trace these effects to the kernel of the forwards operator. They assert that such effects can be avoided only if information about the kernel is encoded into the reconstruction procedure. Based on this, this work aims to spur research into new ways to develop robust and reliable AI-inspired methods for inverse problems in imaging.

Keywords Inverse problems, imaging, deep learning, hallucinations, instability, no-free lunch theorems.

Mathematics Subject Classification (2010): 65R32, 94A08, 68T05, 65M12.

1 Introduction

It is impossible to overstate the impact that Neural Networks (NNs) and Deep Learning (DL) have had in recent years in Machine Learning (ML) applications such as image classification,

*NMG acknowledges support from a UK EPSRC grant. ACH acknowledges support from a Royal Society University Research Fellowship and the Leverhulme Prize 2017. BA acknowledges the support of the PIMS CRG “High-dimensional Data Analysis”, SFU’s Big Data Initiative “Next Big Question” Fund and NSERC through grant R611675.

[†]University of Cambridge, Wilberforce Road, Cambridge CB3 0WA, UK (nmg43@cam.ac.uk)

[‡]University of Oslo, P.O box 1053, Blindern, 0316 Oslo, Norway (vegarant@math.uio.no)

[§]University of Cambridge, Wilberforce Road, Cambridge CB3 0WA, UK (ach70@cam.ac.uk)

[¶]Simon Fraser University, 8888 University Drive Burnaby, BC V5A 1S6, Canada (ben_adcock@sfu.ca)

speech recognition and natural language processing. Perhaps unsurprisingly, the development and use of Artificial Intelligence (AI)-inspired methods for challenging problems in the computational sciences has recently become an active area of inquiry. Areas of particular notice include numerical PDEs [117, 150], discovering PDE dynamics [125], Uncertainty Quantification [23, 57] and high-dimensional approximation [1, 2, 129].

Arguably, however, the area of computational science in which AI-based methods have been most actively investigated is inverse problems in imaging. The task of recovering an image from measurements is of vital importance in a wide range of scientific, industrial and medical applications. These include, but are by no means limited to, electron and fluorescence microscopy, seismic imaging, Nuclear Magnetic Resonance (NMR), Magnetic Resonance Imaging (MRI) and X-Ray Computerized Tomography (CT). In the last several years, there has been an unprecedented amount of activity in the application of ML, and specifically, DL, in this area (see §2.3 for an overview of relevant literature). Given the potential for breakthrough performance, it seems possible that the future of the field lies with AI-inspired algorithms. Notably, their potential has been described by *Nature* as ‘transformative’ [138].¹

1.1 Hallucinations, instability and unpredictable performance

However, there is now increasing awareness that methods in inverse problems – both based on DL and other techniques (see Remark 1.1) – can suffer from (i) *hallucinations*, i.e., realistic-looking artifacts that appear in a reconstructed image that are not present in the ground truth image; (ii) *instabilities*, i.e., sensitivity to perturbations in the measurements; and (iii) *unpredictable performance*, i.e., excellent performance on some images, but significantly worse performance on certain nearby images. For example, in the evaluation of the *2020 Facebook fastMRI challenge* [104], the authors write

“Such hallucinatory features are not acceptable and especially problematic if they mimic normal structures that are either not present or actually abnormal. Neural network models can be unstable as demonstrated via adversarial perturbation studies [10].”

Similarly, in the work *On hallucinations in tomographic image reconstruction* [22]:

“The potential lack of generalization of deep learning-based reconstruction methods as well as their innate unstable nature may cause false structures to appear in the reconstructed image that are absent in the object being imaged.”

Nor are these issues limited to medical imaging. In *Applications, promises, and pitfalls of deep learning for fluorescence image reconstruction* [19], the authors write

“The most serious issue when applying deep learning for discovery is that of hallucination. [...] These hallucinations are deceptive artifacts that appear highly plausible in the absence of contradictory information and can be challenging, if not impossible, to detect.”

and in *The promise and peril of deep learning in microscopy* [71], they write

“However, if the neural network encounters unknown specimens, or known specimens imaged with unknown microscopes, it can produce nonsensical results.”

Similar commentary can also be found in [27, 66, 70, 83, 84, 91, 103, 112, 133, 136, 141, 142, 146, 154, 157]. To highlight this issue, in Fig. 1 we present several examples of AI-based methods for different imaging tasks. In all cases, the recovered images exhibit realistic-looking features that are not present in the corresponding ground truth images. In other words, the reconstruction procedures generate hallucinations.

¹To be specific, [138] is titled ‘AI transforms image reconstruction’ and features a new DL approach [161] which ‘improves speed, accuracy and robustness of biomedical image reconstruction’.

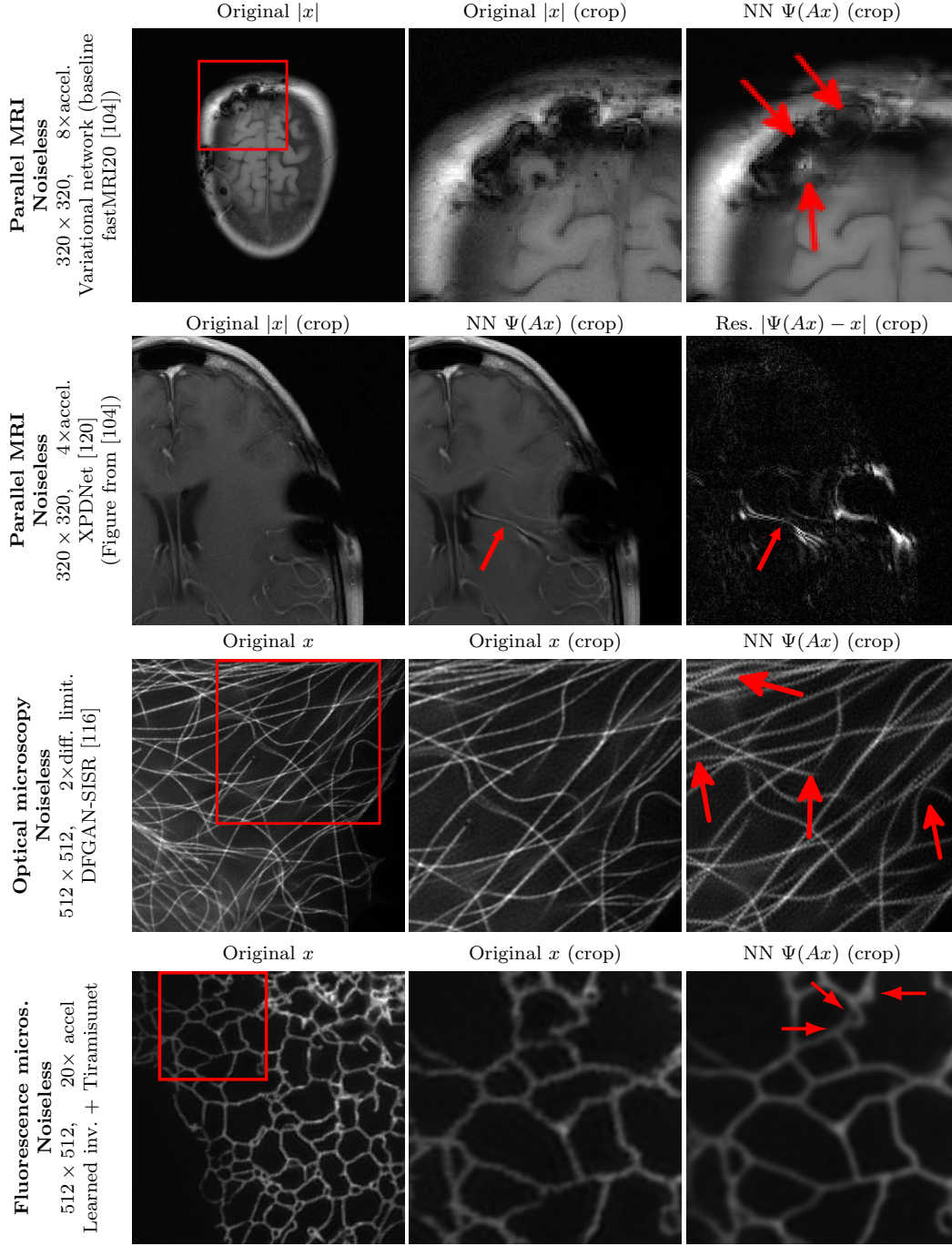


Figure 1: **(AI-generated hallucinations in different imaging modalities).** Trained NNs $\Psi: \mathbb{C}^m \rightarrow \mathbb{R}^N$ for different imaging modalities generate hallucinations, i.e., realistic-looking artifacts, when evaluated on test data. Note that m , N and A vary between the experiments. In the first three rows we consider trained NNs from the cited publications. In row four, we have trained a NN using data from [116]. For more information on the training procedure see §A.

1.2 This paper: hallucinations, no free lunches and the accuracy-stability trade-off

Because of these concerns, there is now a growing research focus on empirically examining the robustness (or lack thereof) and performance of AI-based methods in practical imaging scenarios [10, 41, 49, 59, 72, 75, 103, 104, 112, 133, 157, 158]. The aim of this paper is to provide a theoretical counterpart to these studies by developing a mathematical understanding for how and why such phenomena arise. In particular, we trace the source of these phenomena to the non-trivial kernel of the forwards (sampling) operator in typical imaging scenarios. Described in more detail in §2, our main contribution is a series of theoretical results that describe mechanisms that can cause hallucinations, instabilities or unpredictable performance to occur whenever this kernel is non-trivial. We also present a series of numerical experiments complementing such results, which illustrate these mechanisms in practice.

Our results follow the grand tradition in ML of ‘no free lunch’ theorems [131, 152, 153]. Broadly speaking, our results show that a reconstruction procedure that *overperforms* in a certain sense, must inevitably succumb to one or more of the main phenomena. Several of our results describe a fundamental *accuracy-stability trade-off* for inverse problems, wherein if the accuracy of a method is pushed too far (e.g., by driving the training error to zero), it inevitably becomes unstable.

Remark 1.1 (Are these phenomena exclusive to AI-based methods?). The increasing focus on the pitfalls of DL for imaging has also led researchers in recent years to re-examine standard methods – for example, those based on sparse regularization [3] – more closely from the perspective of performance versus undesirable effects such as hallucinations, instabilities and unpredictable performance. Several works have reported that these methods may also be susceptible to some of these issues [7, 41, 59, 158], albeit arguably in not as dramatic ways that certain AI-based methods can be. We discuss this matter in more detail in §2.3.

The purpose of this work is not to advocate one methodology over the other. Rather, our aim is to develop a series of the theoretical mechanisms that inevitably lead to such undesirable effects. While some of our results are geared towards learning-based methods, most of them apply to arbitrary reconstruction methods, thereby including sparse regularization as a particular case. For example, the accuracy-stability trade-off that we establish – an effect that was observed empirically in several of the aforementioned works [59, 158] – states that *any* method, AI-based or not, that strives to achieve too high accuracy must inevitably become unstable.

1.3 Robustness and trustworthiness in AI

Our work is part of the broader discussion on robustness (or lack thereof) and trustworthiness of AI. This is not just an issue in the computational sciences, but one which affects all sectors in which AI-based techniques are beginning to be actively used. It is notable that the governmental bodies are currently striving to address these concerns. For instance, the European Commission is in the process of outlining a legal framework for the use of AI, with an emphasis on robustness and trustworthiness [48].

Thus, the performance of DL in inverse problems in imaging is a part of a larger, fundamental issue that needs addressing at all levels. The aim of this paper is not to provide solutions to these issues. Yet by exposing the underlying mechanisms that cause hallucinations, instabilities and unpredictable performance, we aim to gain insight into how these issues may be eventually overcome, thus enabling the safe and trustworthy use of DL in computational sciences.

2 Overview of the paper

In this section, we give an overview of the paper. We first formalize the main problem studied, then we give a summary of our main results. Finally, we conclude with a discussion of related literature.

2.1 Problem outline

The concern of this paper is the following discrete inverse problem:

$$\text{Given measurements } y = Ax + e, \text{ recover } x. \quad (2.1)$$

Here $A \in \mathbb{C}^{m \times N}$ is the *sampling operator* (also called *measurement matrix*), $y \in \mathbb{C}^m$ is a vector of *measurements*, $e \in \mathbb{C}^m$ is measurement noise and $x \in \mathbb{C}^N$ is the (unknown) object to recover (typically a discrete image in a vectorized form). While seemingly simple, the model (2.1) is often sufficient to model many applications, including all of those mentioned above. In practice, A is rank deficient, i.e., $1 \leq \text{rank}(A) < N$ and therefore its kernel $\mathcal{A}(A)$ is nontrivial. This makes solving (2.1) a challenge, since, even in the noiseless case $e = 0$, there are infinitely many candidate solutions x that yield the same measurements y .

This paper is about *reconstruction maps* for (2.1). These are mappings of the form $\Psi: \mathbb{C}^m \rightarrow \mathbb{C}^N$ from the measurement domain \mathbb{C}^m to the object domain \mathbb{C}^N . Occasionally, we also allow for multivalued maps, which we denote as $\Psi: \mathbb{C}^m \rightrightarrows \mathbb{C}^N$. To design a reconstruction map for (2.1), one normally assumes that the desired images x belong to some set $\mathcal{M}_1 \subset \mathbb{C}^N$. This set is sometimes referred to as a *model class* or *image manifold*. Thus, rather than solving (2.1), one solves the problem

$$\text{Given measurements } y = Ax + e \text{ of } x \in \mathcal{M}_1, \text{ recover } x. \quad (2.2)$$

Broadly speaking, methods for solving (2.2) can be divided into two types:

- (i) In *model-based* methods, one makes explicit assumptions about \mathcal{M}_1 , and designs the reconstruction map based on the choice of \mathcal{M}_1 . Common choices for \mathcal{M}_1 include sets of images which are approximately sparse in a wavelet basis (or some other multiscale system such as curvelets or shearlets) or images with approximately sparse gradient. To recover $x \in \mathcal{M}_1$, one then usually solves a regularized least-squares problem, typically involving the ℓ^1 -norm.
- (ii) In *learning-based* methods, on the other hand, one makes little or no explicit assumptions about \mathcal{M}_1 . Instead, one is given a *training set* $\mathcal{T} = \{(y_i, x_i)\}_{i=1}^K \subset \mathbb{C}^m \times \mathbb{C}^N$, where $y_i = Ax_i + e_i$ are noisy measurements of x_i (the x_i s often are assumed to be a subset of \mathcal{M}_1). Using this set, one learns a reconstruction map $\hat{\Psi}: \mathbb{C}^m \rightarrow \mathbb{C}^N$ by solving an optimization problem. For instance, given a class \mathcal{NN} of NNs $\varphi: \mathbb{C}^m \rightarrow \mathbb{C}^N$, a regularization term $J: \mathcal{NN} \rightarrow \mathbb{R}_{\geq 0}$ and a regularization parameter $\lambda \geq 0$, a standard choice involves (approximately) solving the regularized training problem

$$\min_{\varphi \in \mathcal{NN}} \frac{1}{|\mathcal{T}|} \sum_{(y,x) \in \mathcal{T}} \frac{1}{2} \|\varphi(y) - x\|^2 + \lambda J(\varphi). \quad (2.3)$$

2.2 Summary of main results

We now present a summary of our main results. For the benefit of the reader, the following statements are phrased in a nontechnical way. See §4 for the formal statements.

Main result 2.1 (Hallucinations due to detail transfer – Theorem 4.1). *Let $x \in \mathbb{C}^N$ and $x_{\text{Det}} \in \mathbb{C}^N$ be a detail that either belongs or lies close to $\mathcal{N}(A)$, i.e., $\|Ax_{\text{Det}}\| \ll 1$ for some norm $\|\cdot\|$. Then the following hold.*

- (i) *Any map Ψ that recovers the detail image $x + x_{\text{Det}}$ will hallucinate by incorrectly transferring this detail when reconstructing the detail-free image x , i.e., $\Psi(Ax + e) \approx x + x_{\text{Det}}$. Thus, a hallucination occurs.*
- (ii) *There always exist NNs (with bounded Lipschitz constants) that can recover details belonging to or close to $\mathcal{N}(A)$. Thus, a NN with small error over a set of images (e.g., the training set) is liable to hallucinate.*

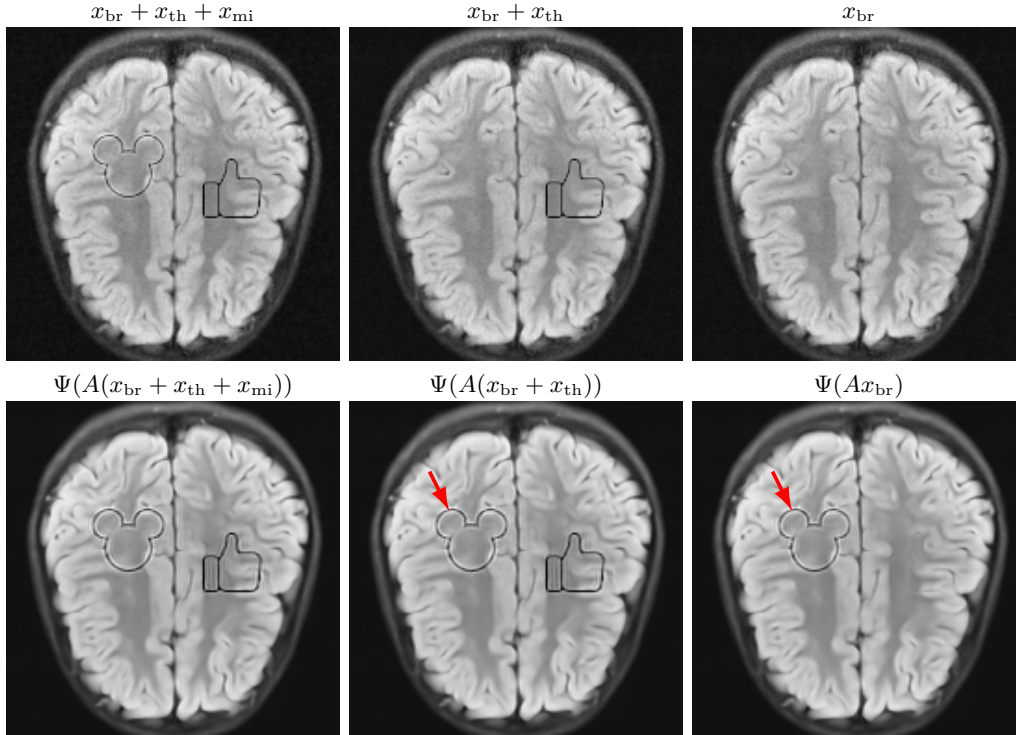


Figure 2: **(Hallucinations due to detail transfer)**. A trained NN $\Psi: \mathbb{C}^m \rightarrow \mathbb{C}^N$ accurately recovers the detail image in the first column. But it hallucinates by incorrectly transferring the ‘Mickey Mouse’ detail x_{mi} in the first column when recovering the images in the second and third column. The measurement matrix is a subsampled Fourier transform with $m/N = 20\%$, which models a MRI acquisition with 5-fold acceleration. See §A for further information on this experiment. Note that the the NN does not transfer the ‘Thumb’ detail x_{th} . Theorems 4.1 and 4.2 sheds light on why this is the case.

The main consequence of this result is that there is an *accuracy-hallucination barrier*. If the map Ψ performs too well on a certain image x_1 with detail lying close to $\mathcal{N}(A)$, then it will hallucinate, by incorrectly transferring this detail to another image x_2 . In Fig. 2 we demonstrate an example of this effect. A NN is trained to accurately recover a brain image with artificial details. Then, when used to reconstruct the detail-free brain image, it hallucinates one of the details. Theorem 4.1 also explains why only one of the details is transferred in this case, and not the other.

Note that the reconstruction map in Main Result 2.1 can be completely stable. In other words, hallucinations are not necessarily a result of instability. As we see below in Main Result 2.3, instability of a reconstruction map can also cause hallucinations, but it is not necessary prerequisite for their appearance.

Main Result 2.1 considers the performance of a reconstruction map on a single image. In our second main result, we consider a more standard training scenario where a reconstruction map is learned to perform well on a class of images.

Main result 2.2 (No free lunch I: overperformance implies hallucinations, yet non-hallucinating algorithms exist – Theorem 4.2). *Suppose that $1 \leq \text{rank}(A) < N$, $\mathcal{T} \subset \mathbb{C}^N$ is a finite set and Ψ is a reconstruction map that achieves small error over \mathcal{T} . Then there are infinitely-many model classes \mathcal{M}_1 with $\mathcal{T} \subset \mathcal{M}_1$ such that Ψ hallucinates on \mathcal{M}_1 with high probability (regardless of the distribution on \mathcal{M}_1). However, there exists an algorithm for computing NNs that achieve small errors on \mathcal{M}_1 and therefore do not hallucinate on \mathcal{M}_1 .*

The main consequence of this result is that hallucinations arise necessarily as a result of overperformance of a reconstruction map that has no knowledge of the model class \mathcal{M}_1 . But if information about \mathcal{M}_1 is given, then there are reconstruction maps – and specifically, NN

reconstruction maps – that do not hallucinate. These NNs can also be computed in finitely-many arithmetic operations and comparisons. Note that the hallucinations described by this result are *in-distribution* hallucinations: namely, $\Psi(Ax) \approx x + x_{\text{Det}}$ for some $x \in \mathcal{M}_1$ belonging to the model class. These are potentially far more problematic than *out-of-distribution* hallucinations.

Main result 2.3 (No free lunch II: over- or inconsistent performance implies both hallucinations and instabilities – Theorem 4.4). *Consider two distinct images x, x' whose difference lies in or close to $\mathcal{N}(A)$. If Ψ recovers both x and x' well (overperformance), or recovers x well and x' poorly (inconsistent performance), then the following must hold.*

- (i) Ψ is unstable in a ball around $y = Ax$, with the instability becoming worse as the reconstruction performance improves.
- (ii) Ψ hallucinates in a ball around $y = Ax$: there are small perturbations e for which, when applied to measurements $Ax + e$, Ψ produces false details not in the image x .

A key consequence of this result is that there is an *accuracy-stability trade-off*. If the reconstruction map Ψ overperforms (on as little as two images) then it is necessarily unstable, with the instability becoming arbitrarily large as the performance increases. This result also asserts that instabilities and hallucinations are *stable*. Bad perturbations do not belong to a set of Lebesgue measure zero. In fact, there are balls of such perturbations. See also Main Result 2.4 below.

Put another way, Main Result 2.3 states that a reconstruction map can only be stable if it does not overperform on certain images. This is a problem for learning-based algorithms, which are typically trained to achieve small error on the training set. According to this result, if there are two images in the training set whose difference lies close to $\mathcal{N}(A)$, then the learned map will necessarily be unstable.

For this reason, successful training should balance stability and performance. In Fig. 3 we show an example of this trade-off, thereby demonstrating Theorem 4.4 in practice. This figure is based on an experiment shown in [59]. Here, training with noiseless measurements yields high performance, but high instability, while training with highly noisy measurements yields high stability, at the expense of significantly worse performance. But this does not need to be only way one may trade-off between these two competing factors. Devising training strategies that optimize the trade-off between performance and stability is a substantial challenge.

Main Result 2.3 asserts the existence of ‘bad’ perturbations that cause either instabilities or hallucinations. A natural question to ask is whether these are rare events. In the next main result, we show that they not need to be.

Main result 2.4 (Instabilities and hallucinations are not rare events – Theorems 4.5 and 4.6). *Consider the same conditions as Main Result 2.3 and let E be an absolutely continuous random vector with a strictly positive probability density function. Then, with nonzero probability,*

- (i) Ψ is unstable, i.e., $\|\Psi(Ax + E) - \Psi(Ax)\| \gg 0$,
- (ii) Ψ hallucinates, i.e., when applied to measurements $Ax + E$, it produces false details not in the image x .

Moreover, for any $0 < \delta < 1$ there is a Gaussian distribution with small mean for which this holds with probability at least $1 - \delta$. Furthermore, subject to several additional conditions, the variance of this Gaussian distribution tends to zero as $m \rightarrow \infty$.

This result implies that random noise can also produce undesirable effects. In Fig. 4 we show several examples of this effect. For the first DL method, mean zero Gaussian noise causes the NN reconstruction map to hallucinate, by artificially removing an image feature (indicated by the red arrow). In the second case, certain *image independent, small mean* Gaussian noise causes severe instabilities in the recovered image. Notice that the noise causes the second DL method to exhibit completely nonphysical artefacts, which could be easily identified by a practitioner as a failure mode. Yet for the first method it creates seemingly realistic artefacts (hallucinations). Such pernicious artefacts may be impossible to detect.

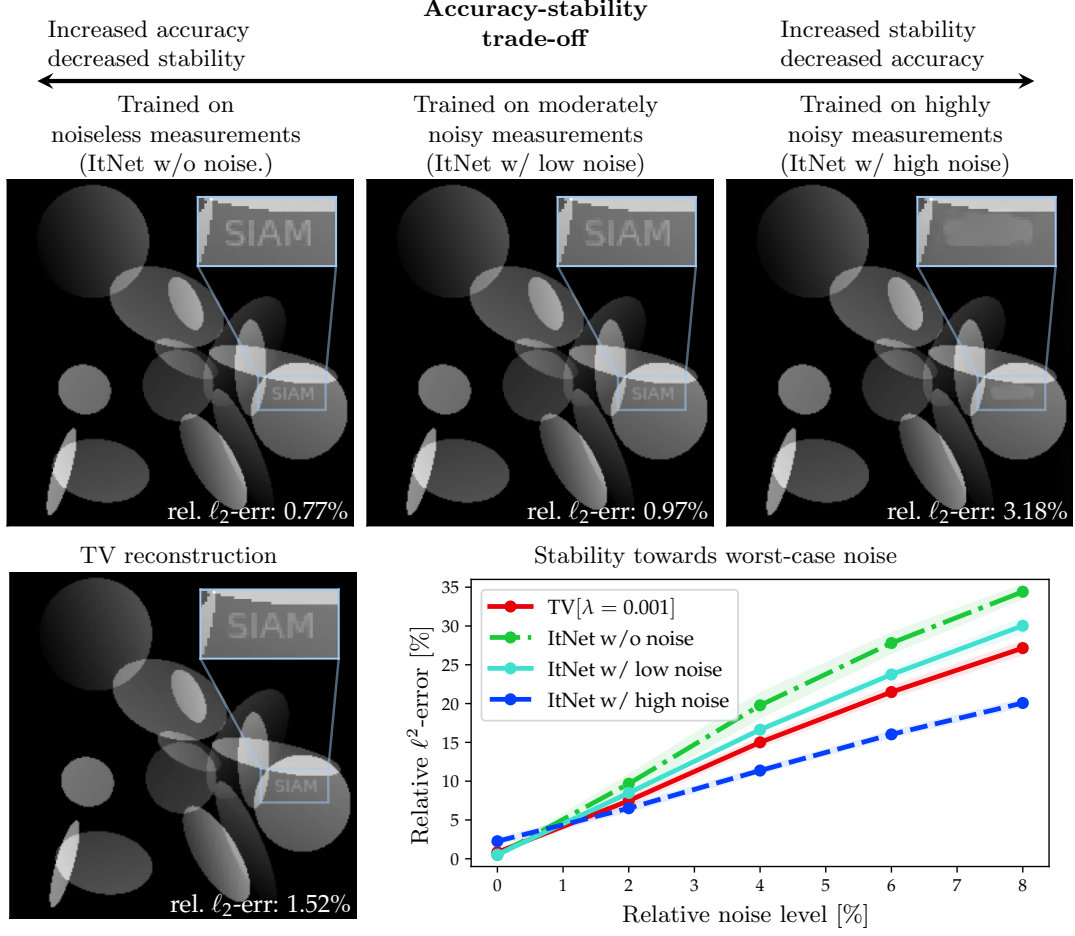


Figure 3: **(The accuracy-stability trade-off)** Three NNs are trained on the same dataset of images with noiseless, low-noise or high-noise measurements, respectively. The NN trained on noiseless measurements has the highest accuracy, but the worst stability, while the NN trained on high-noise measurements has the lower accuracy, but the best stability. The measurement matrix is a subsampled Fourier transform with $m/N \approx 17\%$. For comparison, a model-based reconstruction method based on TV minimization is also included. This experiment is based on one shown in [59]. See §A for further information.

Having considered hallucinations and instabilities, in the next result we switch focus and consider the performance of reconstruction maps in terms of their accuracy (generalization). We do this by following the well established framework of *optimal recovery* (or, as we term it, *optimal maps*). Specifically, we consider the existence of mappings $\Psi: \mathcal{M}_2 = A(\mathcal{M}_1) \rightarrow \mathbb{C}^N$ that achieve the smallest possible worst-case error over a given model class \mathcal{M}_1 . This is a topic with a long history [101], but one that has been the subject of renewed interest in recent years. See the seminal work of Cohen, Dahmen & DeVore [37] and, more recently, [24, 30, 43, 54, 143, 144].

Main result 2.5 (Optimal maps may be impossible to train – Theorem 4.9). *Suppose that A has nontrivial kernel and let $\delta \leq 1/5$. Then the following hold.*

- (i) *There are uncountably many model classes \mathcal{M}_1 and sets \mathcal{T} for which any map Ψ that produces an error of at most δ over \mathcal{T} cannot be an optimal map (or an approximately optimal map) over \mathcal{M}_1 .*
- (ii) *There are uncountably many model classes \mathcal{M}_1 for which no map can attain an error of δ over \mathcal{M}_1 .*

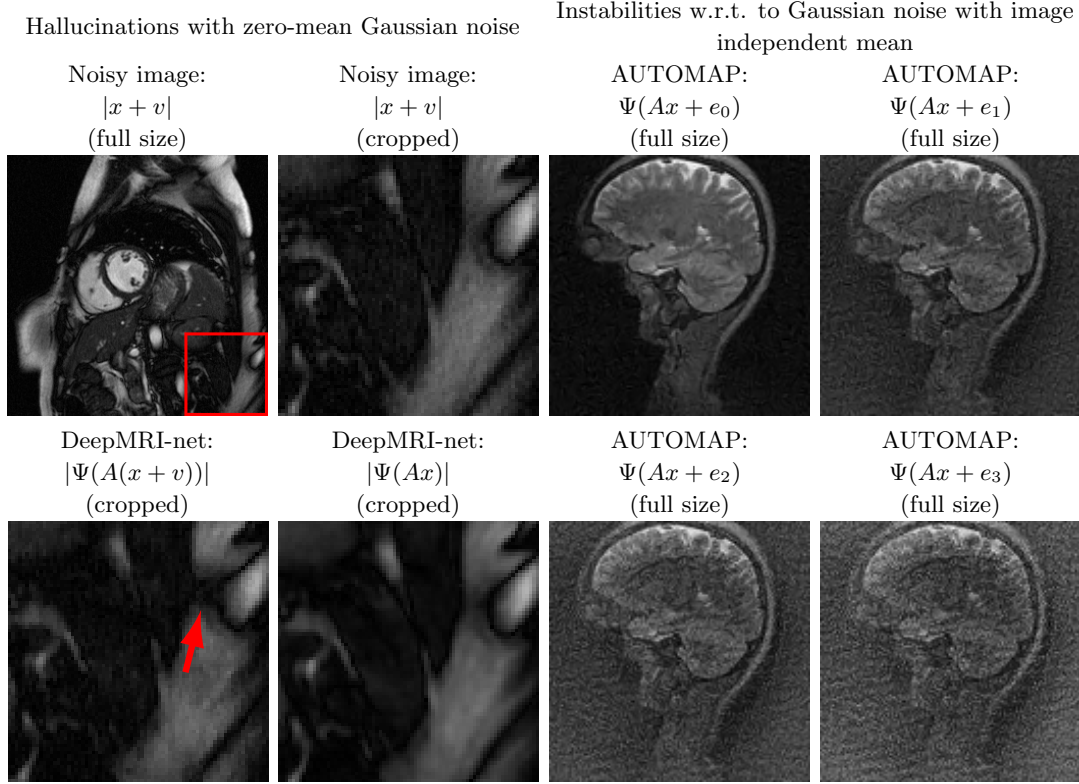


Figure 4: **(Hallucinations and instabilities due to random noise)** Two DL methods exhibit hallucinations and instabilities due to random noise. On the left, the DeepMRI-net [128] reconstruction map is unstable to mean-zero Gaussian noise v . In this case, the NN hallucinates by removing a key image feature (see the red arrow). On the right, the AUTOMAP [161] reconstruction map is unstable to Gaussian noise. The noise vector e_0 is drawn from a zero-mean Gaussian distribution, whereas the mean of the distribution, used to generate e_1, e_2 and e_3 , is based on three worst-case noise vectors computed for AUTOMAP with respect to a different image. This makes the mean is image independent. As we can see, the instability of the map produces noticeable artefacts. The measurement matrix in these experiments is a subsampled Fourier transform with 33% (left) and 60% (right) subsampling, respectively. See §A for further information.

Part (i) of this result asserts that training may fail to yield optimal maps. A small error over \mathcal{T} (which may, for example, correspond to the training set, or the union of the training set and test set) offers no guarantee that the learned map be optimal over the model class. Put another way, the learned map may suffer from *inconsistent* performance. Part (ii) asserts that there are model classes \mathcal{M}_1 for which there is no map that can achieve a small error over \mathcal{M}_1 . In other words, the map (implicitly) sought by training may not exist in the first place.

Thus far, our main results describe various problems that can arise when constructing reconstruction maps for inverse problems. In our final result, we focus on common strategies that one may try to use to improve the performance of DL. These include techniques such as regularization, where, as in (2.3), a penalty term J is added to the loss function. But they also include more sophisticated approaches such as *adversarial training*, and in particular, adversarial training with so-called *Generative Adversarial Networks (GANs)*.

In the following result, we make the additional assumption that the measurement matrix $A \in \mathbb{C}^{m \times N}$ is of the form $P_\Omega U$, where $U \in \mathbb{C}^{N \times N}$ is invertible and P_Ω is a *row selector* matrix which chooses rows of U corresponding to an index set $\Omega \subset \{1, \dots, N\}$ with $|\Omega| = m$. Note that this setup occurs in many practical imaging applications. For example, in MRI U is the matrix of the discrete Fourier transform.

Main result 2.6 (Stability versus performance: setting the regularization parameter is challenging – Theorem 4.12). *Let $U \in \mathbb{C}^{N \times N}$ be invertible. Then there are exponentially many (in N) sampling patterns Ω such that, with $A = P_\Omega U$ there are uncountably many domains \mathcal{M}_1 and uncountably many training sets \mathcal{T} such that there is a choice of the regularization parameter λ for which the set of minimizers of the corresponding training problem contains an optimal map. However, if an element is either added to the training set, or replaces an existing element, then the set of minimizers fails to contain an optimal map.*

This result implies that choosing a good regularization parameter can be very delicate. The performance of DL can be extremely brittle with respect to the training parameter or completely robust, depending on the problem. Ironically, one ends up with a potentially unstable problem in order to cure issues (including instability) that arise in the original training problem.

2.3 Related work

We conclude this section with a discussion on related work.

2.3.1 Traditional image reconstruction methods

Inverse problems in imaging is a vast topic [15, 29, 47, 80, 89, 99, 106], with a history dating back many decades and many different methodologies. Traditional image reconstruction methods are typically model-based. They try to solve (2.2), given an accurate description of A and \mathcal{M}_1 . Here \mathcal{M}_1 could be the subspace $\mathcal{N}(A)^\perp$, or the space of images which are (approximately) sparse in a wavelet or discrete gradient transform (or their various generalizations). In cases where A is poorly conditioned, Tikhonov regularization [140] has been widely used. However, with the advent of compressive sensing [32, 45] in the mid-2000s, sparsity promoting methods using different types of ℓ^1 -regularization gained popularity. These methods allowed practitioners to reduce the sampling rates beyond standard methods at the time, while preserving the reconstruction accuracy. Today, DL-based methods have surpassed the accuracy of all traditional methods. However, recent results have also indicated that traditional methods fine-tuned by using ML can achieve comparable accuracy to DL-based methods for moderate acceleration factors [64]. For recent overviews of traditional methods and more on the transition to data-driven methods, we refer the reader to [3, 98, 121].

2.3.2 AI as a tool for image reconstruction

Image reconstruction is in the process of being transformed by AI and DL. There are already many review articles summarizing recent progress in this area [11, 20, 78, 86, 88, 93, 97, 110, 112, 121, 122, 126, 148, 149]. We do not intend to present an overview of all contributions, but we will highlight a small subset here.

A substantial advance was presented by Jin, McCann, Froustey & Unser in [74]. Here the authors were among the first to use a U-net architecture with a skip connection to reconstruct high-quality sparse view CT images. Since then, the U-net architecture has been widely used in image reconstruction, both as a component of state-of-the-art architectures [58, 76, 92, 119] and as a baseline model [79].

Other works have focused on building network architectures by unrolling optimization algorithms/problems as NNs. This idea dates back to Gregor & LeCun [63], and is celebrated for its ease of interpretation. Important contributions in this direction for image reconstruction were made by Yang, Sun, Li & Xu [156], Adler & Öktem [4, 5], Putzky & Welling [92, 115], Hammernik et al. [65], Mardani et al. [96] and many others. See [11, 102, 121] and [3, Chpts. 20 & 21] for further information on unrolling. Perpendicular to this line of work, Zhu et al. [161] proposed a fully learned approach without guidance from physics. While this approach has been criticized for scaling poorly to high dimensional problems, successful applications using a clever warm start combined with a Kronecker product trick can be found in [59].

Another popular approach has been to reuse image denoising algorithms for image reconstruction. This was first proposed by Venkatakrishnan, Bouman & Wohlberg as the Plug-and-Play

prior method [147], but similar methods, such as Regularization by Denoising (RED) [38, 124], have also been proposed. While these initial methods used handcrafted denoisers, current approaches tend to use NNs, see e.g., [6, 31, 35, 38, 90, 100, 124] and references therein.

Most of the methods mentioned above are based on supervised learning, and rely on large training datasets to attain good performance. However, dataset-independent methods have also been developed. In [145] Ulyanov, Vedaldi & Lempitsky demonstrated the deep image prior approach. This method strives for data consistency, and trains a new NN to reconstruct an image x for each new measurement vector y , without any training data. The method has been explored for image reconstruction in e.g., [13, 68, 69, 109, 141].

A similar, but slightly different approach, based on generative networks, has also been proposed [28] by Bora, Jalal, Price & Dimakis. In their work, they first train a generative network, which then, in turn, is used to generate realistic-looking images agreeing with the measurements y . The method has been developed and analyzed further in [21, 44, 46, 130, 151]. The generative approach and the deep image prior approach have many similarities. For an in-depth overview of these methods and their theoretical guarantees, we refer to the recent paper [127].

Generative models were first developed as part of adversarial training with GANs [61], in which a discriminative network is used as part of the loss function. This has been extended to image reconstruction in many different works, see e.g., [40, 55, 95, 116, 155]. More broadly, one can view the GAN-loss as one particular example of a regularized loss function. Other examples include ℓ^1 or ℓ^2 -loss [128] on the network weights, NNs [94], as well as more exotic options [161], where the ℓ^1 -loss is added directly to the output of certain layers. Traditional adversarial training, where worst-case noise is added to the measurements, has been explored in [36, 118].

Given the tremendous empirical success AI and DL methods have had in image reconstruction in the last few years, a key question these days is whether these methods can actually solve a given inverse problem. That is, given a noiseless training set $\mathcal{T} = \{(Ax^j, x^j)\}_{j=1}^r$, where $x^j \in \mathcal{M}_1$, will these methods find a solution map that can accurately reconstruct the elements in \mathcal{M}_1 . This question has been investigated both from a theoretical and practical perspective for different choices of A and \mathcal{M}_1 . In [134] Sidky, Lorente, Brankov & Pan asked the question in CT for sparse gradient images, with A being a discrete Radon transform. This work later propelled an AAPM Grand Challenge, whose purpose was “*to find the deep-learning (DL) technique for [...] image reconstruction that can yield the minimum root mean square error (RMSE) under ideal conditions*” [135]. The question has also been investigated theoretically in [16, 39], where they show that no algorithm can train NNs to solve certain ℓ^1 -regularized optimization problems to arbitrary accuracy. However, given the right assumptions on A and \mathcal{M}_1 , one can construct efficient NNs with provable guarantees [107].

2.3.3 Instabilities, generalization and hallucinations in AI

The issue of instabilities in DL has been an active area of inquiry ever since Szegedy et al. [139] demonstrated that state-of-the-art deep NNs used in image classification are unstable to certain small adversarial perturbations of the input. By now, the phenomenon seems ever present [17, 67] in most state-of-the-art DL techniques used in, e.g., image classification [50, 52, 81], audio and speech recognition [33, 34], natural language processing [87] and automated diagnosis in medicine [53].

For image reconstruction, the issue of instabilities for DL methods was first investigated empirically in [10, 72]. This was followed by further investigations on the phenomenon in [41, 59], which also included stability tests for sparse regularization decoders and investigations of distribution shifts for both DL and sparsity-promoting methods. A key finding in these works is that both sparse regularization and DL methods are susceptible to worst-case noise and distribution shifts in the data (recall Remark 1.1). However, other results have also suggested robustness of sparse regularization to worse-case noise [39, 107], [3, Chpt. 21]. Thus, different implementations of the sparse regularization strategies may affect their reliability. As was also noted in [158], the instabilities observed in [41] for parallel MRI may also be influenced by the moderate ill-conditioning of the forwards problem for high acceleration factors.

The strategies in [10, 41, 59, 72] are based on finding a worst-case perturbation in the ℓ^2 -norm. Other ‘attack’ strategies have also been proposed. Examples include using NNs to generate the worst-case noise [118], localized attacks [7, 103] or attacks based on rotation [103]. As noted, [59] also empirically studied the accuracy-stability trade-off for DL in imaging (recall Fig. 3).

In [10] it was observed that NNs can be unstable to changing acquisition strategies. In particular, acquiring more samples does not necessarily enhance accuracy when using NNs, unlike with standard methods. This behaviour has been further investigated in [60, 62, 75]. In [60] Gilton, Ongie & Willett developed two strategies to tackle this problem, based on (i) retraining the NN and (ii) a new regularization procedure involving the old NN. In [62] Gossard & Weiss make an empirical investigation of how training on multiple sampling patterns in MRI can improve robustness towards changing acquisition strategies, while in [75] Johnson et al. test the submissions from the 2019 fastMRI challenge with respect to changing acquisition settings.

The issue of robustness toward changing acquisition strategies is closely related to the issue of distribution shifts [123] in ML. That is, how does a method trained on one dataset generalize to a different dataset? This question has received increased attention [41, 104, 133, 157] in imaging, as DL-based methods are now entering clinical practice [56, 113]. In [133] Shimron, Tamir, Wang & Lustig study how common ML training pipelines can lead to models that are biased towards the training data, whereas [157] investigates the generalizability of self-supervised methods for both prospective and retrospective MRI data. In [41] they investigate distribution shifts for learning and model-based methods. The 2020 fastMRI challenge also introduced a test to check a NN’s ability to generalize on data from different MRI scanners [104].

As highlighted in §1, the issue of AI-generated hallucinations is raising concerns within the imaging community. Hallucinations have the potential to cause misdiagnoses in medicine [22, 79, 104] and to hinder discoveries in the life sciences [19, 71]. To simplify research on hallucinations in medical imaging, the fastMRI+ [159] and SKM-TEA [42] datasets have recently been introduced. These datasets contain expert annotations of relevant pathologies and thereby allow practitioners to automate the search for hallucinations in reconstructed images [12, 77, 160]. It has also become customary to test different models’ ability to reconstruct unseen features in the images, by adding small details not contained in the training dataset, see e.g., [75, Fig. 2], [82, Fig. 6.8] and [110, Fig. 12]. This test was initially proposed in [10].

It is also worth noting that several generative models have been shown to hallucinate. In the landmark publication [28], one can, for example, see in Fig. 15c how the generative model puts red lipstick on a man’s lips and draw eyes on top of sunglasses. Furthermore, in [73, Fig. 3] one can see how different generative reconstruction algorithms produce nonsensical, but realistic-looking faces when the matrix A and measurements y are corrupted by noise. While the issue of hallucinations is not the focus of these works, it shows that this phenomenon is pervasive.

3 Preliminaries

Before stating our main results, some comments on notation are in order. Given a set $\mathcal{M}_1 \subset \mathbb{C}^N$ and a matrix $A \in \mathbb{C}^{m \times N}$, we let $\mathcal{M}_2 = A\mathcal{M}_1 = \{Ax : x \in \mathcal{M}_1\}$ denote the range of A with domain \mathcal{M}_1 . For a set $\Omega \subset \{1, \dots, N\}$, we let $P_\Omega \in \mathbb{C}^{N \times N}$ denote the projection onto the canonical basis indexed by Ω , i.e., for $x \in \mathbb{C}^N$, $(P_\Omega x)_i = x_i$ if $i \in \Omega$ and 0 otherwise. We sometimes abuse notation slightly and assume that $P_\Omega \in \mathbb{C}^{m \times N}$, where $m = |\Omega|$, by ignoring the zero entries.

Throughout we let $\|\cdot\|$ denote a norm on \mathbb{C}^N and $|||\cdot|||$ denote a norm on \mathbb{C}^m . We let $\mathcal{B}(x, r) = \{z \in \mathbb{C}^N : \|x - z\| \leq r\}$ denote the closed ball centered at $x \in \mathbb{C}^N$ with radius $r > 0$. If $x \in \mathbb{C}^m$, then $\mathcal{B}(x, r) \subset \mathbb{C}^m$ denotes a ball centred at x with radius r in the norm $|||\cdot|||$. For a set $\mathcal{M}_1 \subset \mathbb{C}^N$, we use the notation

$$\mathcal{M}_1^\nu = \{z \in \mathbb{C}^N : \exists x \in \mathcal{M}_1 \text{ such that } \|z - x\| < \nu\}$$

to denote the ν -neighborhood of \mathcal{M}_1 in \mathbb{C}^N . The notation is extended in the natural way to \mathcal{M}_2^ν for $\mathcal{M}_2 \subset \mathbb{C}^m$.

For $\epsilon > 0$ and $y \in \mathbb{C}^m$, we define the local ϵ -Lipschitz constant of a mapping $\Phi: \mathbb{C}^m \rightarrow \mathbb{C}^N$ as

$$L^\epsilon(\Phi, y) = \sup_{\substack{z \in \mathbb{C}^m \\ 0 < \|z - y\| \leq \epsilon}} \frac{\|\Phi(z) - \Phi(y)\|}{\|z - y\|}.$$

We also write

$$L(\Phi) = \sup_{\substack{y, z \in \mathbb{C}^m \\ z \neq y}} \frac{\|\Phi(z) - \Phi(y)\|}{\|z - y\|}$$

for its global Lipschitz constant.

In this work, we consider, standard *feedforward* NNs. An L -layer feedforward NN is a function $\Psi: \mathbb{R}^{m'} \rightarrow \mathbb{R}^{N'}$ of the form

$$\Psi(y) = V_L(\rho(V_{L-1}(\rho(\dots \rho(V_1(y)))))), \quad y \in \mathbb{R}^{m'}, \quad (3.1)$$

where each $V_j: \mathbb{R}^{n_{j-1}} \rightarrow \mathbb{R}^{n_j}$ is an affine map, i.e.,

$$V_j x = W_j x + b_j, \quad x \in \mathbb{R}^{n_{j-1}},$$

for $W_j \in \mathbb{R}^{n_j \times n_{j-1}}$, $b_j \in \mathbb{R}^{n_j}$, $\rho: \mathbb{R} \rightarrow \mathbb{R}$ is a non-linear function, $\rho(x) = (\rho(x_i))$ for $x = (x_i)$ and $n_0 = m'$, $n_L = N'$. The W_j s are referred to as *weights* and the b_j s as *biases*. The number L is the *depth* of the network, and n_l is the *width* of its l th layer. The function ρ is the *activation function*. Typical choices for ρ are the *Rectified Linear Unit (ReLU)*, defined by $\rho(y) = \max\{0, y\}$, or the *sigmoid*, defined by $\rho(y) = \frac{1}{1+e^{-y}}$. The *architecture* of a neural network refers to choice of the depth L , widths n_1, \dots, n_{L-1} and activation function ρ . The class of neural networks with a given architecture is denoted as \mathcal{NN} or $\mathcal{NN}_{\mathbf{n}}$, where $\mathbf{n} = (n_0, n_1, \dots, n_L)$.

In inverse problems (typically MRI), it is common to deal with complex input $y \in \mathbb{C}^m$ and output $x \in \mathbb{C}^N$. Conversely, NNs are typically real-valued functions. A standard way to resolve this is to associate $y \in \mathbb{C}^m$ with $\hat{y} \in \mathbb{R}^{2m}$, apply a real-valued NN $\Psi: \mathbb{R}^{2m} \rightarrow \mathbb{R}^{2N}$ and then associate the output $\hat{x} = \Psi(\hat{y})$ with a complex image $x \in \mathbb{C}^N$. We assume the complex case is treated in this way throughout this paper. Henceforth we simply write $\Psi: \mathbb{C}^m \rightarrow \mathbb{C}^N$ for a network taking complex inputs and outputs, with the assumption that it has this form.

For many imaging modalities, the noise is modelled as a complex random variable drawn from a complex normal distribution. This is denoted by $\mathbb{CN}(v, \Sigma)$, where $v \in \mathbb{C}^m$ is the mean and $\Sigma \in \mathbb{C}^{m \times m}$ is the positive semi-definite covariance matrix. We note that the probability density function of $\mathbb{CN}(v, \Sigma)$ exists if Σ is positive definite and it is given by [8, Thm. 2.10]

$$\pi^{-m} \det(\Sigma)^{-1} \exp(-(u - v)^* \Sigma^{-1} (u - v)), \quad u \in \mathbb{C}^m.$$

For an in-depth introduction to complex random variables and complex normal distributions see the excellent book by Andersen, Højbjerg, Sørensen & Eriksen [8].

4 Main results

In this section, we state our main results. Proofs can be found in the appendix.

4.1 Hallucinations due to detail transfer

Recall that a *hallucination* is a realistic-looking, but ultimately false detail that arises in a reconstructed image. There are various mechanism that can cause hallucinations, one of which is *detail transfer*. Detail transfer means that a detail from one image – typically, in the case of DL, this is an element of the training set from which the NN reconstruction map is learned – is transferred to another image via the reconstruction map. See Fig. 2 for an illustration of this process. In the following theorem, we provide a mathematical rationale for hallucinations arising via detail transfer.

Theorem 4.1. *Let $A \in \mathbb{C}^{m \times N}$, $\delta > 0$ and $x, x_{\text{Det}} \in \mathbb{C}^N$ with $\|Ax_{\text{Det}}\| \leq \delta$.*

(i) (Ψ hallucinates by transferring details). Let $\Psi: \mathbb{C}^m \rightarrow \mathbb{C}^N$ be Lipschitz continuous with constant at most $L > 0$ and suppose that

$$\|\Psi(A(x + x_{\text{Det}})) - (x + x_{\text{Det}})\| \leq \delta. \quad (4.1)$$

Then for every $e \in \mathcal{B}(0, \delta)$, there is a $z \in \mathbb{C}^N$ with $\|z\| \leq (1 + 2L)\delta$, such that

$$\Psi(Ax + e) = x + x_{\text{Det}} + z.$$

(ii) (There always exists a DNN that hallucinates). For any choice of depth $K > 1$, internal dimensions n_1, \dots, n_{K-1} and activation function ρ , there is a NN of the form (3.1) with Lipschitz constant at most L that satisfies (4.1).

Let $\delta > 0$ be some small number. Then this theorem asserts that the detail x_{Det} in the image $x' := x + x_{\text{Det}}$ will be transferred onto the detail-free image x given noisy (or noiseless) measurements $Ax + e$, with $e \in \mathcal{B}(0, \delta)$. Note that this theorem does not require a formal definition of what constitutes a detail. Clearly, this theorem is most relevant in the case where $\|x_{\text{Det}}\| \gg \delta \geq \|Ax_{\text{Det}}\|$. In other words, the detail is significant (large in norm), but has small measurements. Informally, a detail x_{Det} should also be a ‘local’ feature, whose presence or absence is clearly visible. A ‘global’ feature, such as a texture, may not be noticeable, even if relatively large in norm.

Fig. 2 presents an example of this result. In this figure, the ‘Mickey Mouse’ detail $x_{\text{mi}} \in \mathcal{N}(A)$, whereas the ‘Thumb’ detail x_{th} has relatively large measurements, i.e., $\|Ax_{\text{th}}\| \gg 0$. The NN is trained to recover the image $x_{\text{br}} + x_{\text{th}} + x_{\text{mi}}$. As a result, it incorrectly transfers the detail x_{mi} , while the detail x_{th} is handled correctly (i.e., it is not transferred).

Observe that Theorem 4.1 does not require the map Ψ to be unstable. It arises because detail x_{Det} lies close to the kernel of A , i.e., $\|Ax_{\text{Det}}\| \leq \delta$, and the reconstruction map Ψ recovers x' well. Since the measurements $y' = Ax'$ and $y = Ax + e$ are similar, i.e., $\|y - y'\| \leq 2\delta$, the Lipschitz continuity of Ψ means that it must, when presented with measurements y , produce an image that is close to x' .

Theorem 4.1 also shows how alarmingly easy it is for a reconstruction map to hallucinate. Simply recovering an image with a detail x_{Det} lying close to $\mathcal{N}(A)$ is enough for hallucinations to arise. Measurement matrices in imaging problems typically have large kernels. For example, in MRI one may often consider images of size $N = 256 \times 256 = 65536$ and a subsampling factor of 25%, giving $m = 16384$ measurements. Hence $\mathcal{N}(A)$ has dimension $N - m = 49152$. Therefore, given a training set of typical MRI images, the large dimension of $\mathcal{N}(A)$ means there may well be many possible ways in which the conditions that lead to part (i) of Theorem 4.1 can arise.

Part (ii) of Theorem 4.1 suggests that hallucinations due to detail transfer can occur very easily in, for instance, DL. If a NN is trained using a training set that contains images with details x_{Det} – for instance, small tumours or lesions in the case of medical imaging – lying close to the kernel of A , then it will be liable to hallucinate such details when subsequently applied to images outside of the training set that lack this detail. Put another way, Ψ may produce *false positives*. Or, if the scenario is reversed, it may produce *false negatives*. Both effects are highly undesirable in, for instance, a medical imaging scenario.

4.2 No free lunch I: overperformance implies hallucinations, yet non-hallucinating algorithms exist

Since the previous theorem is very general, the question arises as to how it relates to learning-based methods – i.e., those that use a training set to learn a reconstruction map – for solving inverse problems. The following theorem elaborates on this relation.

Theorem 4.2. Let $A \in \mathbb{C}^{m \times N}$ with $1 \leq \text{rank}(A) < N$, $\mathcal{T} \subset \mathbb{C}^N$ be a non-empty and finite set, $\delta > 0$, $\Psi: \mathbb{C}^m \rightarrow \mathbb{C}^N$ be a NN with Lipschitz constant $L > 0$ and $x_{\text{Det}} \in \mathbb{C}^N$ with $\|Ax_{\text{Det}}\| \leq \delta/(4L)$. Suppose that Ψ satisfies

$$\max_{x \in \mathcal{T}} \|\Psi(Ax) - x\| \leq \delta.$$

Then, for any $\epsilon \geq \delta/(2L)$ there is an uncountable family \mathcal{C} of finite and countably infinite sets $\mathcal{M}_1 \subset \mathbb{C}^N$ with $\mathcal{T} \subset \mathcal{M}_1$ and $A\mathcal{M}_1 \subset (AT)^\epsilon$, such that for each $\mathcal{M}_1 \in \mathcal{C}$ the following hold simultaneously.

- (i) (Ψ suffers from in-distribution hallucinations). For any probability distribution \mathcal{D} on \mathcal{M}_1 with the property that $\mathbb{P}_{X \sim \mathcal{D}}(X \in \mathcal{T}) \leq q$, it holds that

$$\mathbb{P}_{X \sim \mathcal{D}}\left(\exists \lambda \in \mathbb{C}, |\lambda| = 1 \text{ such that } \|\Psi(AX) - (X + \lambda x_{\text{Det}})\| \leq 2\delta\right) \geq 1 - q.$$

- (ii) (There exists an algorithm that yields non-hallucinating NNs). There exists an algorithm Γ taking inputs in $A(\mathcal{M}_1)$ such that, for each $y \in A(\mathcal{M}_1)$, $\Gamma(y) = \Phi_y$ is a NN $\Phi_y : \mathbb{C}^m \rightarrow \mathbb{C}^N$ that satisfies

$$\|\Phi_{Ax}(Ax) - x\| \leq \delta, \forall x \in \mathcal{M}_1.$$

Note that the assumption that Ψ is a NN is only needed for part (ii) of the statement. Part (i) holds for any Lipschitz continuous reconstruction map $\Psi : \mathbb{C}^m \rightarrow \mathbb{C}^N$. Part (i) of this theorem therefore says that a reconstruction map that *overperforms* on a set \mathcal{T} (e.g., a training set) that belongs to a model class \mathcal{M}_1 must, with high probability, hallucinate over \mathcal{M}_1 . We refer to these as *in-distribution* hallucinations, since the inputs X which suffer from hallucinations are drawn from a distribution over \mathcal{M}_1 . Recall that a model class \mathcal{M}_1 represents the images we are interested in recovering in a given application. For example, these may be brain images in MRI. Thus, while *out-of-distribution* hallucinations may not be problematic in practice, in-distribution hallucinations are far more worrying.

Part (i) of Theorem 4.2 is general in that it holds for any distribution \mathcal{D} , with the only assumption being that $\mathbb{P}_{X \sim \mathcal{D}}(X \in \mathcal{T}) \leq q$. In other words, the set \mathcal{T} cannot have too large a measure relative to \mathcal{M}_1 and \mathcal{D} . The main consequence of this result is that hallucinations of this type cannot be avoided when using standard NN training strategies that simply strive for small error over a training set. Put another way, to prevent against such hallucinations, it is necessary to change the training strategy to incorporate additional information about the problem.

This brings us to part (ii) of the theorem. It states that there is an algorithm for computing NN reconstruction maps that achieve hallucination-free performance over \mathcal{M}_1 . Note that by ‘algorithm’ we mean that Γ takes a finite set of real numbers as its input (i.e., the vector y) and perform only finitely-many arithmetic operations and comparisons, producing a finite set of real numbers as its output (i.e., the weights and biases of a NN). More formally, Γ is a BSS (Blum-Shub-Smale) machine – see the proof of Theorem 4.2 for details.

The key point is that, as opposed to a single NN Ψ as in part (i), in part (ii) we allow the NN Φ_y to depend on the input. Note that this idea is not far-fetched. In fact, NNs that arise from unrolling optimization algorithms [102], [3, Chpt. 21] and NNs based on the deep image prior framework [127, 145] are generally of this type.

Remark 4.3. Theorem 4.2 is *not* a statement about overfitting. Overfitting in DL occurs when a NN performs well on the training set, but poorly on the test set. This phenomenon is caused by the fact that the architecture of the network are fixed, and hence its ability to fit data is limited (it can fit the training set, but not the test set). It is a classical result in approximation theory that any set of data points (e.g. the union of the training and test sets) can be interpolated by a NN of sufficient size [114]. So even if the trained network would suffer from overfitting, and hence lack performance on the test set, there will exist another NN that interpolates all data points in the training set as well as the test set. What Theorem 4.2 describes is a phenomenon that happens *for all* mappings. There is no restriction in the network architecture, and, in fact, in part (i) Ψ need not be a NN in the first place. More directly, one could simply let the set \mathcal{T} in part (i) contain both the training sets and test sets. Theorem 4.2 then says that one can have excellent performance on these sets but still suffer from in-distribution hallucinations.

4.3 No free lunch II: over- or inconsistent performance implies both hallucinations and instabilities

In the previous results, we described how overperformance can cause hallucinations. We now describe a second key mechanism that can cause a reconstruction map to perform in a substandard way. In the following result, we show that *over- or inconsistent performance* of a reconstruction map causes both instabilities and hallucinations.

Theorem 4.4. *Let $A \in \mathbb{C}^{m \times N}$, $x, x' \in \mathbb{C}^N$ and $\eta > 0$. Let $\Psi: \mathbb{C}^m \rightarrow \mathbb{C}^N$ be continuous and suppose that*

$$\|\Psi(Ax) - x\| < \eta, \quad \|\Psi(Ax') - x''\| < \eta, \quad (4.2)$$

for some $x'' \in \mathbb{C}^N$ and that

$$\|Ax - Ax'\| \leq \eta. \quad (4.3)$$

Then the following hold:

- (i) (Ψ is unstable). *There is a closed non-empty ball $\mathcal{B} \subset \mathbb{C}^m$ centred at $y = Ax$ such that, for all $\epsilon \geq \eta$, the local ϵ -Lipschitz constant at any $\tilde{y} \in \mathcal{B}$ satisfies*

$$L^\epsilon(\Psi, \tilde{y}) \geq \frac{1}{\eta} (\|x - x''\| - 2\eta). \quad (4.4)$$

- (ii) (Ψ hallucinates). *There exist $z \in \mathbb{C}^N$ with $\|z\| \geq \|x - x''\|$ (for example, $z = x'' - x$), $e \in \mathbb{C}^m$ with $\|e\| \leq \eta$, and closed non-empty balls \mathcal{B}_x , \mathcal{B}_e and \mathcal{B}_z centred at x , e and z respectively such that*

$$\|\Psi(A\tilde{x} + \tilde{e}) - (\tilde{x} + \tilde{z})\| \leq \eta, \quad \forall \tilde{x} \in \mathcal{B}_x, \tilde{e} \in \mathcal{B}_e, \tilde{z} \in \mathcal{B}_z. \quad (4.5)$$

Suppose first that $x'' = x'$, so that the map Ψ reconstructs both x and x' to within an accuracy of η . Suppose also that x and x' are sufficiently distinct, i.e., $\|x - x'\| > 2\eta$. Then (4.2)-(4.3) state that Ψ *overperforms* in the sense that it recovers two vectors x, x' well whose difference lies close to the kernel of A . In other words, Ψ strives to get something from nothing: the x and x' are distinct, but their measurements are similar. The result, unsurprisingly, is instability, with the local Lipschitz constant in a ball around $y = Ax$ scaling like $1/\eta$. And the more the reconstruction map overperforms, the worse this instability becomes.

Now suppose that x' is close to x , but $\|x - x''\| > 2\eta$. In this case, Ψ performs *inconsistently*: it recovers x well, but recovers a nearby x' poorly. Once more, the conclusion is the same: Ψ is necessarily unstable in a ball around $y = Ax$.

The second implication of (4.2)-(4.3) is that Ψ hallucinates. To see this, it is convenient to rewrite x' as $x' = x + x_{\text{Det}}$. Assume for simplicity that $x'' = x'$. Then (4.2) states that Ψ recovers both x and $x + x_{\text{Det}}$ well, where, due to (4.3), the detail x_{Det} lies close to the kernel of A . Part (ii) of Theorem 4.4 now asserts that Ψ hallucinates. There exists a small perturbation e with $\|e\| \leq \eta$ such that, for example, $\Psi(Ax + e)$ is within η of $x' = x + x_{\text{Det}}$. Thus, a small perturbation of the measurements of the detail-free image x causes Ψ to falsely reconstruct the image x' containing the detail. It consequently yields a false positive. Moreover, the result is stable, in the sense that it holds not just for x, x' and e , but for any vectors lying in balls around them. Note also that it is not necessary for Ψ to overperform in order for it to hallucinate. If (4.3) holds for some x'' that is not close to x , then (ii) implies hallucinations, in the sense that there are perturbations for which $\Psi(Ax + e) \approx x''$.

The conditions of Theorem 4.4 are very general, since they pertain to the performance of Ψ on two elements only. Moreover, overperformance in the above sense can arise easily when training a DNN. Indeed, if the training set contains two elements (Ax, x) and (Ax', x') for which (4.3) holds, then a small training error implies (4.2). Similarly, inconsistent performance can occur whenever x belongs to the training set and x' is close to this set, but not in it.

4.4 Instabilities and hallucinations are not rare events

Theorem 4.4 asserts the existence of ‘bad’ perturbations, which cause either instabilities or hallucinations. It says nothing about how prevalent such bad perturbations are. However, the fact the various conclusions of Theorem 4.4 hold in balls implies that these are not rare events. We formalize this statement in the following theorem.

Theorem 4.5. *Let $A \in \mathbb{C}^{m \times N}$, $x, x' \in \mathbb{C}^N$ and $\eta > 0$. Let $\Psi: \mathbb{C}^m \rightarrow \mathbb{C}^N$ be continuous and suppose that Ψ satisfies (4.2)–(4.3) for some $x'' \in \mathbb{C}^N$. If $E = \{E_1, \dots, E_m\}$ is an absolutely continuous complex-valued random vector with a strictly positive probability density function, then the following hold.*

- (i) (Instabilities are not necessarily rare events). *There is a closed ball $\mathcal{B}_x \subset \mathbb{C}^N$ centred at x and a $c > 0$ such that*

$$\mathbb{P}(\|\Psi(A\tilde{x} + E) - \Psi(A\tilde{x})\| \geq \|x - x''\| - 2\eta) \geq c, \quad \forall \tilde{x} \in \mathcal{B}_x. \quad (4.6)$$

Moreover, for any $0 < \delta < 1$, there is a complex Gaussian distribution on E whose mean has norm at most η such that (4.6) holds with $c = 1 - \delta$.

- (ii) (Hallucinations are not necessarily rare events). *There is a $c > 0$ and $z \in \mathbb{C}^N$ with $\|z\| \geq \|x - x''\|$ (for example, $z = x'' - x$), and closed balls $\mathcal{B}_x, \mathcal{B}_z \subset \mathbb{C}^N$, centred at x and z , respectively, such that*

$$\mathbb{P}(\|\Psi(A\tilde{x} + E) - (\tilde{x} + \tilde{z})\| \leq \eta) \geq c, \quad \forall \tilde{x} \in \mathcal{B}_x, \tilde{z} \in \mathcal{B}_z. \quad (4.7)$$

Moreover, for any $0 < \delta < 1$, there is a complex Gaussian distribution on E whose mean has norm at most η such that (4.7) holds with $c = 1 - \delta$.

This result shows that instabilities and hallucinations are not rare events. If the perturbation is drawn randomly from an arbitrary distribution, the probability of it causing a hallucination or instability is non-zero. Furthermore, this occurs with high probability for Gaussian noise with small mean. Note that Gaussian noise is ubiquitous in imaging applications.

A limitation of this result is that it makes no claims as to the size of the variance of the Gaussian noise for which its conclusions hold. However, under somewhat more restrictive conditions one can show that similar effects occur for Gaussian noise of arbitrarily-small variance as $m \rightarrow \infty$.

Theorem 4.6 (Worst-case variance tends to zero). *Let $\|\cdot\|$ and $\|\cdot\|$ be equal to the Euclidean norm $\|\cdot\|_{\ell^2}$. Let $U \in \mathbb{C}^{N \times N}$ be unitary, $\Omega \subset \{1, \dots, N\}$ with $m = |\Omega|$ and $A = P_\Omega U$. Let $x, x' \in \mathbb{C}^N$, $\eta, \delta, \sigma > 0$ and $\Psi: \mathbb{C}^m \rightarrow \mathbb{C}^N$ be continuous. Suppose that $\|\Psi(Ax) - x\|_{\ell^2} < \eta$, $\|Ax' - Ax\|_{\ell^2} > \delta$ and that, for every $\tilde{x}' \in \mathcal{B}(x', \delta)$ there is a $x'' \in \mathbb{C}^N$ such that*

$$\|\Psi(A\tilde{x}') - x''\|_{\ell^2} < \eta. \quad (4.8)$$

Denote the union of all such x'' s by \mathcal{S} . Let $\xi \in \mathbb{C}^m$ and $I \in \mathbb{C}^{m \times m}$ be the identity matrix. Then, if $E \sim \mathbb{CN}(\xi, \sigma^2 I)$ we have that

$$\begin{aligned} & \mathbb{P} \left(\|\Psi(Ax + E) - \Psi(Ax)\|_{\ell^2} \geq \inf_{x'' \in \mathcal{S}} \|x - x''\|_{\ell^2} - 2\eta \right) \\ & \geq (\pi\sigma^2)^{-m} \int_{\mathcal{B}} \exp \left(-\frac{1}{\sigma^2} \|t - \xi\|_{\ell^2}^2 \right) dt \end{aligned} \quad (4.9)$$

where $\mathcal{B} := \mathcal{B}(Ax' - Ax, \delta)$. Moreover, there exists a variance $\sigma_0 = \sigma_0(m)$ maximizing the lower bound in (4.9), such that $\sigma_0(m) \rightarrow 0$ as $m, N \rightarrow \infty$ for fixed Ω, x, x', δ and ξ . Furthermore, if $\|Ax' - Ax - \xi\|_{\ell^2} < \delta$ then

$$\mathbb{P} \left(\|\Psi(Ax + E) - \Psi(Ax)\|_{\ell^2} \geq \inf_{x'' \in \mathcal{S}} \|x - x''\|_{\ell^2} - 2\eta \right) \rightarrow 1,$$

as $m \rightarrow \infty$ whenever $\sigma = \sigma(m) \leq \sigma_0(m)$.

4.5 Optimal maps may be impossible to train

In this section, we switch focus and consider optimal recovery via the notion of *optimal maps*. This study is motivated by the following question: given an inverse problem and a model class \mathcal{M}_1 , what is the best possible reconstruction map? Note that we consider noiseless measurements in this section, in order to focus the discussion on the underlying accuracy of a recover. It is possible to extend such considerations to the noisy regime [30, 143].

In order to maintain sufficient generality, in this section we consider multivalued maps. Doing so allows one to consider standard approaches, such as sparse regularization, that rely on minimizers of convex optimization problems which need not be unique. Recall that a multivalued map is typically denoted with double arrows. Thus, in this section, we consider maps of the form

$$\Psi : \mathcal{M}_2 \rightrightarrows \mathbb{C}^N,$$

where $\mathcal{M}_2 = A(\mathcal{M}_1)$. We assume that the set $\Psi(y)$ is bounded for all $y \in \mathcal{M}_2$. To measure distance between two bounded sets $X, Z \subset \mathbb{C}^N$, we use the Hausdorff distance. If d is a metric on \mathbb{C}^N then this is defined by

$$d^H(Z, X) = \max \left\{ \sup_{x \in X} \inf_{z \in Z} d(z, x), \sup_{z \in Z} \inf_{x \in X} d(z, x) \right\}.$$

With slight abuse of notation we will denote a singleton $\{x\} \subset \mathcal{M}_1$ simply as x .

Definition 4.7 (Optimal map). Let d be a metric on \mathbb{C}^N , $\mathcal{M}_1 \subset \mathbb{C}^N$, $A \in \mathbb{C}^{m \times N}$ and $\mathcal{M}_2 = A(\mathcal{M}_1)$. The optimality constant of (A, \mathcal{M}_1) is defined as

$$c_{\text{opt}}(A, \mathcal{M}_1) = \inf_{\Psi : \mathcal{M}_2 \rightrightarrows \mathbb{C}^N} \sup_{x \in \mathcal{M}_1} d^H(\Psi(Ax), x). \quad (4.10)$$

A map $\Psi : \mathcal{M}_2 \rightrightarrows \mathbb{C}^N$ is an optimal map for (A, \mathcal{M}_1) if it attains this infimum.

An optimal map is the best possible reconstruction map for a given sampling operator A and model class \mathcal{M}_1 . However, such a map may not exist, since the infimum in (4.10) may not be attained. This motivates the following.

Definition 4.8 (Approximately optimal maps). Let d be a metric on \mathbb{C}^N , $\mathcal{M}_1 \subset \mathbb{C}^N$, $A \in \mathbb{C}^{m \times N}$ and $\mathcal{M}_2 = A(\mathcal{M}_1)$. A family of approximately optimal maps for (A, \mathcal{M}_1) is a collection of maps $\Psi_\epsilon : \mathcal{M}_2 \rightrightarrows \mathbb{C}^N$, $\epsilon \in (0, 1]$, such that

$$\sup_{x \in \mathcal{M}_1} d^H(\Psi_\epsilon(Ax), x) \leq c_{\text{opt}}(A, \mathcal{M}_1) + \epsilon, \quad \forall \epsilon \in (0, 1]. \quad (4.11)$$

Consider a pair (A, \mathcal{M}_1) . In the next result, we address whether or not training gives rise to optimal or approximately optimal maps. Our main conclusion is that it generally does not.

Theorem 4.9 (Absence of optimal maps). *Let the metric d be induced by the norm $\|\cdot\|$, $A \in \mathbb{C}^{m \times N}$ with $1 \leq \text{rank}(A) < N$, $K \in \{2, \dots, \infty\}$, $\delta \leq 1/5$ and let $\mathcal{B} \subset \mathbb{C}^N$ be the closed unit ball with respect to d . Then the following hold.*

- (i) (Training may not yield optimal maps). *There exist uncountably many $\mathcal{M}_1 \subset \mathcal{B}$, such that for each \mathcal{M}_1 there exist countably many sets $\mathcal{T} \subset A(\mathcal{M}_1) \times \mathcal{M}_1$ with $|\mathcal{T}| = K$, where $\mathcal{M}_2 = A(\mathcal{M}_1)$, with the following properties. Any map $\Psi : \mathcal{M}_2 \rightarrow \mathbb{C}^N$ (potentially multivalued $\Psi : \mathcal{M}_2 \rightrightarrows \mathbb{C}^N$) that satisfies*

$$d^H(\Psi(y), x) \leq \delta, \quad \forall (y, x) \in \mathcal{T}, \quad (4.12)$$

is not an optimal map. Moreover, the collection of such mappings does not contain a family of approximate optimal maps. If K is finite, one can choose $|\mathcal{M}_1| = K + 1$, in which case there is at least one \mathcal{T} with the above property.

- (ii) (The map sought by training may not exist). *There exist uncountably many $\mathcal{M}_1 \subset \mathcal{B}$ with $|\mathcal{M}_1| = K$ such that, for $\mathcal{M}_2 = A(\mathcal{M}_1)$, there does not exist a map $\Psi : \mathcal{M}_2 \rightarrow \mathbb{C}^N$ (nor a multivalued map $\Psi : \mathcal{M}_2 \rightrightarrows \mathbb{C}^N$) for which*

$$d^H(\Psi(y), x) \leq \delta, \quad \forall (y = Ax, x) \in \mathcal{M}_2 \times \mathcal{M}_1.$$

A well-trained reconstruction map Ψ should satisfy (4.12) for a suitable δ and some suitable collection of images \mathcal{T} (e.g., the training or test set, or a subset thereof). Thus, part (i) of this theorem states that successful training may not yield an optimal map or an approximately optimal map. Furthermore, part (ii) shows that it may not be possible to achieve a small error over of \mathcal{M}_1 in the first place – i.e., there are model classes that cannot be (implicitly) learned. We remark in passing that the (mild) condition $\delta \leq 1/5$ is related to the assumption that \mathcal{M}_1 is a subset of the unit ball \mathcal{B} . The theorem holds for arbitrary $\delta > 0$, provided this ball is suitably enlarged.

Much like Theorem 4.2, Theorem 4.9 is not simply a statement about overfitting (Remark 4.3 also applies in this case). In particular, Theorem 4.9 implies that Ψ can have excellent performance on both the training and test sets but still be suboptimal.

Remark 4.10. To understand Theorem 4.9 better, it is worth contrasting it with the case of classification. Consider a binary classification problem with an unknown ground truth labelling function $f : \mathcal{M} \rightarrow \{\pm 1\}$. This implies that the training data

$$\{(x_i, f(x_i))\}_{i=1}^K$$

consists of a finite subset of the graph

$$\{(x, f(x)) : x \in \mathcal{M}\}$$

of this function. Thus, in DL for classification, we learn a NN approximation to f from a finite sample of its graph.

By contrast, in an inverse problem the training set takes the form

$$\{(Ax_i, x_i)\}_{i=1}^K. \quad (4.13)$$

However, part (ii) of Theorem 4.9 implies that this generally does not correspond to a finite subset of the graph $\{(y, \Phi(y)) : y \in \mathcal{M}_2\}$ of some optimal (or approximately optimal) map Φ . Thus, there is no reason why training should yield an optimal or approximately optimal map, since the training data (4.13) is not sampled from the graph of such a map. Indeed, this is exactly what is asserted in part (i) of the theorem.

Why does this scenario arise? The answer lies with nontrivial kernel of A . If $A \in \mathbb{C}^{N \times N}$ is invertible, then an optimal map is simply $f(y) = A^{-1}y$, and the training data (4.13) is indeed a subset of the graph of f . Unfortunately, as discussed, this scenario is usually not relevant in modern applications.

4.6 Stability versus performance: setting the regularization parameter is challenging

We have now seen a variety of results that assert the potential for hallucinations (Theorems 4.1 and 4.2), instabilities (Theorems 4.4, 4.5 and 4.6) and suboptimal and/or inconsistent performance (Theorem 4.9). In our final result, we consider a standard set of techniques one may use to try to improve the performance of DL in any of these respects.

To be precise, we now consider learning via the following optimization problem

$$\min_{\varphi \in \mathcal{NN}} \max_{J \in \mathcal{K}} \frac{1}{|\mathcal{T}|} \sum_{(y,x) \in \mathcal{T}} \frac{1}{|\mathcal{T}|} \sum_{x \in \mathcal{T}} \frac{1}{2} \|\varphi(y) - x\|^2 + \lambda J(\varphi, \mathcal{T}). \quad (4.14)$$

Here \mathcal{NN} is a class of NNs $\varphi : \mathbb{C}^m \rightarrow \mathbb{C}^N$, $\lambda \geq 0$ is a regularization parameter, $J : \mathcal{NN} \times \mathcal{E} \rightarrow \mathbb{R}_{\geq 0}$ is a regularization term, where \mathcal{E} is some family of training data, and \mathcal{K} is a suitable class of functions such that the maximum is attained.

The model (4.14) is quite general. It includes standard regularization (2.3), in which case $\mathcal{K} = \{J\}$ is a singleton and $J: \mathcal{NN} \rightarrow \mathbb{R}_{\geq 0}$ is independent of \mathcal{T} . However, it also includes techniques such as adversarial training. Indeed, consider a class of functions \mathcal{L} of the form $L: \mathcal{NN} \times \mathbb{C}^m \rightarrow \mathbb{C}^m$. Then we define the regularization term

$$J_L(\varphi, \mathcal{T}) = \frac{1}{|\mathcal{T}|} \sum_{(y,x) \in \mathcal{T}} \frac{1}{2} \|\varphi(y + L(\varphi, y)) - x\|^2,$$

and the class $\mathcal{K} = \{J_L : L \in \mathcal{L}\}$. In this case, (4.14) becomes a game between two adversaries. One tries to find a NN that performs well over the training set, and the other tries to counteract this by finding worst-case perturbations $L(\varphi, y)$ for each y with $(y, x) \in \mathcal{T}$. Note that a particular instance of this setup is adversarial training with GANs [118]. In this case, NNs are also used to construct the bad perturbations. Thus, \mathcal{L} is chosen as a family of NNs, typically with norm bounded by a certain constant based on the anticipated noise level of the problem.

Regardless of the particular choices of \mathcal{NN} and \mathcal{K} , a fundamental question when solving (4.14) is how does one set the regularization parameter λ ? This question is the focus of this section. For this, we require the following.

Definition 4.11 (Optimal λ). Given a pair (A, \mathcal{M}_1) , classes \mathcal{NN} and \mathcal{K} and a training set \mathcal{T} , we say that $\lambda \in \mathbb{R}_+$ is optimal for $\{(A, \mathcal{M}_1), \mathcal{NN}, \mathcal{K}, \mathcal{T}\}$ if there is a minimizer of (4.14) that is an optimal map for (A, \mathcal{M}_1) .

As the following result reveals, setting the right λ is a highly delicate, and ironically, highly unstable problem.

Theorem 4.12. *Let $U \in \mathbb{C}^{N \times N}$ be an invertible matrix with $N \geq 4$. Then there exist $2^N - 2N - 2$ sampling patterns $\tilde{\Omega} \subset \{1, \dots, N\}$ and for each of them a sampling pattern $\Omega \subset \{1, \dots, N\}$, $|\Omega| \neq N$, such that the following holds for $A = P_\Omega U$ and $\tilde{A} = P_{\tilde{\Omega}} U$. Let $M \in \{2, \dots, \infty\}$, $m = \max\{|\Omega|, |\tilde{\Omega}|\}$ (see Remark 4.13), $\mathcal{NN} = \mathcal{NN}_{\mathbf{n}}$ be any class of ReLU NNs with at least one hidden layer, where $\mathbf{n} = (m, n_1, \dots, n_{L-1}, N)$, $n_j \geq 2m$, in the real case and $\mathbf{n} = (2m, n_1, \dots, n_{L-1}, 2N)$, $n_j \geq 4m$, in the complex case, and consider (4.14). Then there is a $\lambda_{\text{opt}} \in \mathbb{R}_+$ and uncountably many model classes \mathcal{M}_1 of size M such that for each \mathcal{M}_1 there are training sets*

$$\mathcal{T} = \{(Ax_i, x_i)\}_{i=1}^K \subset A(\mathcal{M}_1) \times \mathcal{M}_1, \quad \tilde{\mathcal{T}} = \{(\tilde{A}\tilde{x}_i, \tilde{x}_i)\}_{i=1}^{\tilde{K}} \subset \tilde{A}(\mathcal{M}_1) \times \mathcal{M}_1$$

with $K, \tilde{K} < \infty$ and possibly with $\{x_i\}_{i=1}^K = \{\tilde{x}_i\}_{i=1}^{\tilde{K}}$, for which λ_{opt} is optimal for $\{(\tilde{A}, \mathcal{M}_1), \mathcal{NN}, \mathcal{K}, \tilde{\mathcal{T}}\}$ and $\{(A, \mathcal{M}_1), \mathcal{NN}, \mathcal{K}, \mathcal{T}\}$. However, there exists an uncountable set $\mathcal{S} \subseteq \mathbb{C}^N$ such that the following holds:

- (i) (The sampling pattern $\tilde{\Omega}$ makes λ_{opt} unstable with respect to \mathcal{S}). If $(\tilde{A}x, x)$, $x \in \mathcal{S}$, is either added to the training set $\tilde{\mathcal{T}}$, or replaces a specific element in $\tilde{\mathcal{T}}$, then either there is no element of

$$\operatorname{argmin}_{\varphi \in \mathcal{NN}} \max_{J \in \mathcal{K}} \frac{1}{|\tilde{\mathcal{T}}|} \sum_{(\tilde{y}, \tilde{x}) \in \tilde{\mathcal{T}}} \frac{1}{2} \|\varphi(\tilde{y}) - \tilde{x}\|^2 + \lambda J(\varphi, \mathcal{T}), \quad (4.15)$$

that is an optimal map for $(\tilde{A}, \mathcal{M}_1)$ for any $0 \leq \lambda < \infty$, or there is another $\tilde{\lambda}_{\text{opt}} \neq \lambda_{\text{opt}}$ that is optimal for $\{(\tilde{A}, \mathcal{M}_1), \mathcal{NN}, \mathcal{K}, \tilde{\mathcal{T}}\}$ whereas λ_{opt} is not.

- (ii) (The sampling pattern Ω makes λ_{opt} stable with respect to \mathcal{S}). Given any subset $\mathcal{V} \subset \mathcal{S}$, if $\{(Ax, x) | x \in \mathcal{V}\}$ is either added to \mathcal{T} or replaces elements in \mathcal{T} , then λ_{opt} is still optimal for $\{(A, \mathcal{M}_1), \mathcal{NN}, \mathcal{K}, \mathcal{T}\}$.

Remark 4.13. Note that in the case where $|\Omega| \neq |\tilde{\Omega}|$, we assume the NN first φ zero pads the input to length $m = \max\{|\Omega|, |\tilde{\Omega}|\}$ (in the real case) or $2m$ (in the complex case) as needed.

Theorem 4.12 says that there is an abundance of sampling patterns Ω and $\tilde{\Omega}$, training sets \mathcal{T} and $\tilde{\mathcal{T}}$ and a large set \mathcal{S} for which the following holds. Setting the parameter λ is highly unstable with respect to changes in the training set $\tilde{\mathcal{T}}$ from elements in \mathcal{S} when considering the sampling pattern $\tilde{\Omega}$. Yet, at the same time, setting the parameter λ is highly stable with respect to changes in the training set \mathcal{T} from the same elements in \mathcal{S} when considering the sampling pattern Ω . Hence, changes in the training sets from the same collection \mathcal{S} can give vastly different results. The conclusion is therefore that unless one has prior information about the training data, or a potential way of learning this information, setting the λ parameter is a delicate affair. The irony is that regularization and adversarial training are commonly used to improve the performance of DL with regards to stability or other aspects of performance. However, as Theorem 4.12 asserts, they can potentially result in unstable problems themselves.

5 Conclusions and prospects

This paper strived to provide theoretical explanations for the growing concerns surrounding the use of AI-based methods for inverse problems in imaging. Our main results describe mathematical mechanisms that cause reconstruction maps to hallucinate, become unstable or, in a general sense, perform in an unpredictable or inconsistent manner. While the motivations for this work were AI-based methods, we reiterate at this stage that many of our results are general, and therefore apply to more standard methods (recall Remark 1.1). Nevertheless, our findings indicate that learning-based methods may be especially susceptible to such phenomena. For example, training can easily lead to *overperformance*, yielding instabilities and hallucinations. How to best balance this *accuracy-stability trade-off* while learning is a key problem for future investigations.

We end this paper with a discussion of the broader context and future prospects.

5.1 Adversarial perturbations and instabilities in AI

When adversarial attacks and instabilities were first discovered in late 2013 for image classification [139], the general sentiment for many years that this issue would be quickly solved. This sentiment is maybe best exemplified by Turing Award laureate Geoffrey Hinton’s famous quote “*They should stop training radiologists now.*” (The New Yorker, 2017) [105]. Yet, what happened in the aftermath of Szegedy et al’s [139] discovery was an arms race between those developing new defence strategies and those developing new attack algorithms [111]. While this has spurred many new developments and insights into the robustness of DL methods for decision problems, it has also largely left the problem of developing stable DL classifiers open.

5.2 AI for computational imaging

In much of the same way, the rapid developments in computational imaging have sometimes led to grand claims of robustness, new attack strategies, and conflicting results. There are, for example, no lack of works claiming to solve the issue of instabilities and/or hallucinations. To mention a few, the Nature publication [161] promises “*superior immunity to noise and a reduction in reconstruction artefacts compared with conventional hand-crafted reconstruction methods*”. However, this claim stands in stark contrast to the findings in [10, Fig. 3], showing that the proposed method is severely unstable to worst-case noise. Others have claimed that “*the reconstructed images from NeRP are more robust and reliable, and can capture the small structural changes such as tumor or lesion progression.*” [132], or that “*The concept of deep image prior (DIP) [...] is not affected by the aforementioned instabilities and hallucinations*” [141], or “*It is important to emphasize that the proposed GANCS scheme controls/avoids hallucination by modifying the conventional GAN in the following ways [...]*” [95].

At the same time, there have been numerous works demonstrating how easy it is to fool [7, 10, 41, 59, 72, 103] modern reconstruction methods, either by adding worst-case noise or adding tiny unseen details to the test data. Image reconstruction competitions such as the fastMRI challenges have also found that many of the best-performing algorithms can hallucinate [79, 104],

and that they produced overly smoothed images when higher noise levels were used [75]. To us, this suggests that the question of how to avoid hallucinations is very much an open problem.

5.3 Towards robust AI for computational imaging

For inverse problems, the conclusions of these studies and this paper are decidedly mixed: current approaches to training cannot ensure robust methods; even if they do, the resulting methods may not offer state-of-the-art performance; regularization or adversarial training may not fix these issues. Furthermore, these are not rare events, able to be dismissed by all, but a small group of theoreticians (recall Fig. 4). Should one therefore give up on the AI-based approaches for inverse problems? Of course not. The potential for significant performance gains is too tempting to be dismissed.

It is worth noting the current active research effort to enhance robustness. As observed, simple strategies such as adding random noise to the measurements can encourage learning stable reconstruction maps. However, as discussed (see Fig. 3), optimally balancing *accuracy-stability* trade-off with this approach is by no means straightforward. Other approaches include enforcing data consistency [77, 128] or using *interval NNs (INNs)* [108] or Bayesian approaches [14, 85] to quantify the uncertainty in reconstructed images. While promising, it is currently unclear whether any of these approaches adequately resolve current concerns.

As we observed in §1.1, there are increasing warnings that, if issues such as hallucinations and instabilities cannot be brought under control, the eventual adoption of such techniques in safety-critical applications such as medical imaging may be less than the current optimism suggests. Therefore, our hope is that the findings in this paper – in particular, the crucial role that the kernel of the measurement matrix plays in the performance – will spur new research into devising better ways to design and train robust and reliable AI-based methods for computational imaging.

A Additional information on the figures and experiments

In this section we provide additional information on how the figures were created. In some of the figures we have trained the NNs ourselves. For these NNs, all accompanying code can be found on the GitHub page: https://github.com/vegarant/troublesome_kernel For the NNs which have been trained and published by others, we provide details on which data we have used.

A.1 Fig. 1

Fig. 1 consists of four rows with different NNs tested on different data. In the first row, we downloaded the baseline model used in the 2020 fastMRI challenge [104]. This baseline model is based on a variational NN [137], and trained on the brain image dataset used in the competition. For further details on the training procedure and data used to train this model, we refer to [104]. In our experiment, we used the pseudo-equispaced sampling pattern with 8X acceleration and the 12th slice from the “file_brain_AXT1PRE_200_6002079.h5” file in the validation dataset.

In the second row of Fig. 1, we used a set of images published in the 2020 fastMRI challenge paper [104]. These images are reconstructions created by the XPDNet [120] trained for 4X acceleration.

In row three we consider the DFGAN-SISR model from [116]. This NN has been trained on a dataset consisting of pairs of low and high-resolution microscopy images provided by [116]. In our experiment, we used the DFGAN-SISR model trained for 2X upscaling of MicroTubules (MTs) images from a diffraction-limited wide-field view. For each specimen and each imaging modality in [116], the authors collected 50 pairs of low-resolution (512×512 pixels) and high-resolution (1024×1024 pixels) images. These images were then augmented using random cropping, horizontal/vertical flipping and rotation to generate a dataset of more than 20,000 image pairs of size 128×128 and 256×256 . We have uploaded the relevant input and output images used in row 3 in Fig. 1 to the GitHub repository. For further details on the NN and training procedure, we refer to [116].

In the fourth row, the sampling operator $A \in \mathbb{R}^{m \times N}$ is a subsampled two-dimensional Hadamard transform with $m/N = 5\%$. The sampling pattern is shown in Fig. 6. We trained a Tiramisu NN from [59] with a learnable inverse layer initialized to the adjoint of the sampling operator before training. The NN was first trained for 15 epochs with random Gaussian noise added to the measurements, then for another 10 epochs with noiseless measurements. For training, we used the Adam optimizer and a mean-squared-error loss function. The training data consisted of 10,000 images (of size 512×512 pixels) from the Endoplasmic Reticulum (ER) images acquired in [116]. These 10,000 images were created by running the data-augmentation script provided in [116] on the high-resolution images in this dataset.

A.2 Fig. 2

In Fig. 2, we trained a NN $\Psi: \mathbb{C}^m \rightarrow \mathbb{C}^N$ to reconstruct the image $x = x_{\text{br}} + x_{\text{th}} + x_{\text{mi}} \in \mathbb{C}^N$, along with 1200 other images from the fastMRI brain dataset. Here x_{br} is the brain image seen in the figure, x_{th} is the thumb detail and x_{mi} is the Mickey Mouse detail. The sampling operator $A \in \mathbb{C}^{m \times N}$ used in the experiment was a subsampled two-dimensional Fourier transform with $m/N = 20\%$. The sampling pattern is shown in Fig. 6. The Mickey Mouse detail x_{mi} was designed so that $x_{\text{mi}} \in \mathcal{N}(A)$.

The ground truth images in the fastMRI dataset consist of magnitude images of size 320×320 . In our experiments, we resized these images to 256×256 pixels and stored them as real-valued images with pixel values in the interval $[0, 1]$. The detail x_{mi} is complex-valued, so any image with this detail is necessarily stored as a complex-valued image. To create the input data for the NN, we synthetically sampled these images with the sampling operator described above.

The NN $\Psi(y) = \varphi(A^*y)$ used a U-net $\varphi: \mathbb{C}^N \rightarrow \mathbb{C}^N$ combined with the adjoint A^* of the sampling operator. The NN was trained in two phases. First, we trained the NN for 500 epochs with random Gaussian noise added to the measurements. Then we ran a fine-tuning phase for 100 epochs with noiseless measurements. We used the Adam optimizer with a gradually decaying learning rate (see the GitHub page for details) and a mean-squared-error loss function.

The image $x = x_{\text{br}} + x_{\text{th}} + x_{\text{mi}}$ was part of the training set, whereas the images $x_{\text{br}} + x_{\text{th}}$ and x_{br} were not. In Fig. 2 we have cropped the images to 180×180 pixels to remove some dark areas surrounding the brain.

A.3 Fig. 3

In Fig. 3 we trained three NNs on a dataset consisting of 25,000 ellipses images of size 256×256 . All the NNs have the same architecture, consisting of a cascade of U-Nets and learnable data-consistency layers. This architecture is identical to the ItNet in [59] and resembles the state-of-the-art architecture used in [58] for CT reconstruction. In our experiments we used a subsampled Fourier transform as our sampling operator $A \in \mathbb{C}^{m \times N}$, with $m/N \approx 17\%$ and the sampling pattern shown in Fig. 6, consisting of 40 radial lines.

We trained the NNs using a mean-squared-error loss function and noisy inputs. The technique of adding noise to the input is known as jittering in the machine learning literature. We refer to the intensity of the noise as the jittering level. At jittering level $p > 0$ we drew – for each noiseless measurement vector y and for each epoch of training – a number $s \sim \text{Unif}([0, p])$ from the uniform distribution on $[0, p]$ and a noise vector $e \sim \mathcal{CN}(0, \frac{1}{2}I)$, which we then used to generate the noisy measurements

$$\tilde{y} \leftarrow y + \frac{s}{\sqrt{m}}e.$$

The NNs were trained in different stages and for varying levels of jittering. In the first stage, we trained a simple U-Net to reconstruct the images using a jittering level of $p = 10$. In the second stage, we trained NNs with the architecture described above consisting of a cascade of U-Nets and data-consistency layers. The NN weights of these U-Nets were initialized using the U-Net from the first stage. At this stage, two of the NNs were trained at jittering level 10, whereas the last NN was trained without any jittering. In Fig. 3, we refer to the NN trained without any jittering as the NN trained without noise. Furthermore, one of the NNs trained at jittering level 10 is referred to as the NN trained with high levels of noise. The weights of the other NN trained at jittering level 10 were used as a warm start for the NN trained with low levels of noise. This NN was trained another time, in a third stage, using a jittering level of $1/10$. The training strategy of these three networks is identical to the training procedure used in [59, Fig. 14].

The fourth reconstruction method used in Fig. 3 is based on TV-minimization. That is, we consider the optimization problem

$$\min_{z \in \mathbb{C}^N} \lambda \|\nabla z\|_{\ell^1} + \|Az - y\|_{\ell^2}^2, \quad \lambda > 0,$$

where ∇ is the discrete gradient operator, and we solve this problem using the ADMM algorithm [18, Chpt. 15]. In our experiments we used $\lambda = 0.001$ and ran the algorithm with 5000 iterations. Note that this approach is different from [59] in that we keep λ fixed in all experiments, whereas in [59] this parameter is adjusted according to the noise level. In our experience, setting λ small typically yields high accuracy on this dataset, whereas a larger λ leads to a more stable reconstruction (in an ℓ^2 sense). We found that $\lambda = 0.001$ was a good compromise between the two.

In Fig. 3, we test the stability and accuracy of different reconstruction. To test the accuracy of these methods, we insert the “SIAM” text feature in one of the test images and reconstruct this image from noiseless measurements. None of the NNs have been trained on images with text in them, yet two of the NNs reconstruct this text feature with high accuracy. The NN that fails to reconstruct this text feature is the one trained at the highest noise level. As the text feature has a constant intensity, it is unsurprising that the TV-minimization algorithm reconstructs the feature.

In the graph in Fig. 3 we test the stability of different methods’ towards worst-case noise at different noise levels. This is done as follows. For each reconstruction method, we consider 10 images and the noise levels $\eta = 0, 0.02, 0.04, 0.06, 0.08$. For each image x , noise level η and reconstruction method Ψ , we compute a worst-case perturbation

$$e^{\text{worst}} \in \text{argmax}_{e \in \mathbb{C}^m} \|\Psi(Ax + e) - x\|_{\ell^2}^2 \quad \text{subject to} \quad \|e\|_{\ell^2} \leq \eta \|x\|_{\ell^2}$$

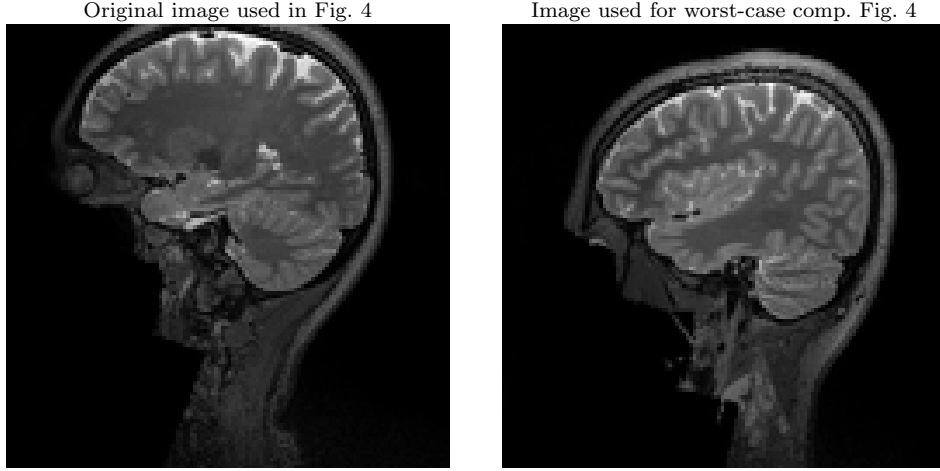


Figure 5: Left: the original image x in Fig. 4. Right: the image that was used to compute the worst-case perturbations $e_{\text{pert},j}^1$ that were subsequently used as the mean of the Gaussian distributions in Fig. 4.

using a projected gradient descent algorithm. The figure shows the average relative reconstruction error at each noise level. The wider shaded areas of each colour indicate the boundaries for one standard deviation of the relative reconstruction error for the considered dataset of 10 images.

A.4 Fig. 4

This Fig. consists of two experiments with two different NNs. We cover both in turn.

In the four leftmost images, we consider the DeepMRI-Net from [128]. This NN is composed of a cascade of U-Nets and data consistency layers. It has been trained on cardiac images, such as the one shown in the figure. The sampling operator A is a subsampled two-dimensional Fourier transform, whose sampling pattern is shown in Fig. 6. The noise vector v used in the experiment was created as $v = A^*e$, where $e \in \mathbb{C}^m$ is a zero-mean complex-valued Gaussian noise vector. Since the mean of a Gaussian random variable is unchanged by a linear transformation, the noise vector v still has zero-mean.

The four rightmost images are from [9]. Code is available at https://github.com/vegarant/automap_not_robust_v2. Here we consider the AUTOMAP network from [161]. This NN was trained by the authors of [161] on brain images from the MGH-USC dataset [51]. It was trained using Fourier sampling with 60% subsampling. In [9], the perturbations

$$e_j = e_{\text{pert},j}^1 + e_{\text{pert},j}^2 \in \mathbb{C}^m, \quad \text{for } j = 0, 1, 2, 3.$$

Here $e_{\text{pert},0}^1 = 0$, and $e_{\text{pert},j}^2$, $j = 0, \dots, 3$ are zero-mean Gaussian vectors. The vectors $e_{\text{pert},j}^1$, $j = 1, 2, 3$, are worst-case noise vectors computed for an image that differs from the image x used in the experiment. This makes the mean of the Gaussian noise vector e_j image independent. The image used to compute the worst-case perturbations $e_{\text{pert},j}^1$ is shown in Fig. 5.

B Proofs of the main results

In the following sections we provide proofs of our main results.

B.1 Proofs of the Theorem 4.1 and Theorem 4.2

Proof of Theorem 4.1. For part (i), let $e \in \mathcal{B}(0, \delta)$. We have that

$$\Psi(Ax + e) = \Psi(A(x + x_{\text{Det}}) + (e - Ax_{\text{Det}})) = \Psi(A(x + x_{\text{Det}})) + z',$$

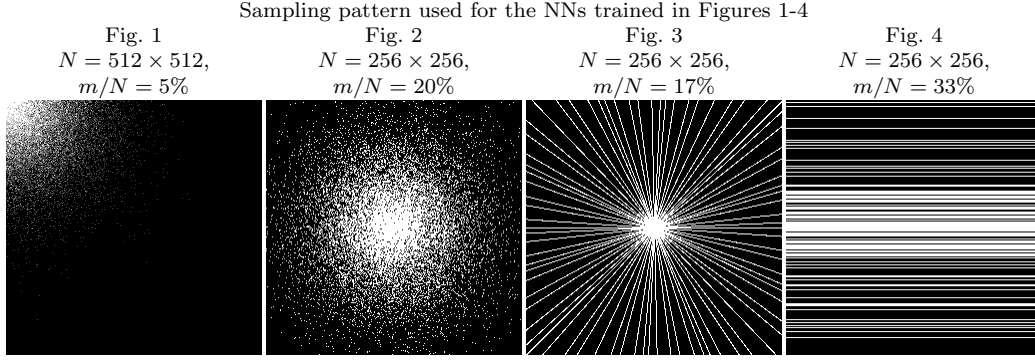


Figure 6: In Figures 1-4 we have trained our own NNs. In this figure we visualize the different sampling patterns used for training of these NNs. Note that the leftmost sampling pattern is used for Hadamard sampling, whereas the three others are used for Fourier sampling.

where

$$\begin{aligned} \|z'\| &= \|\Psi(A(x + x_{\text{Det}}) + (e - Ax_{\text{Det}})) - \Psi(A(x + x_{\text{Det}}))\| \\ &\leq L\|e - Ax_{\text{Det}}\| \leq 2L\delta. \end{aligned}$$

Furthermore, by assumption we have that

$$\Psi(A(x + x_{\text{Det}})) = x + x_{\text{Det}} + \tilde{z},$$

where

$$\|\tilde{z}\| = \|\Psi(A(x + x_{\text{Det}})) - (x + x_{\text{Det}})\| \leq \delta.$$

Combining the above, we get that

$$\Psi(Ax + e) = x + x_{\text{Det}} + z_e,$$

where $\|z_e\| = \|z' + \tilde{z}\| \leq (1 + 2L)\delta$.

Next consider part (ii) and let $z = \hat{x} + \hat{x}_{\text{Det}} \in \mathbb{R}^{2N}$ denote the real version of $x + x_{\text{Det}}$. We will construct a NN satisfying the required conditions as follows. Let $\Phi: \mathbb{R}^{2m} \rightarrow \mathbb{R}^{2N}$ be a K -layer NN, with internal dimensions n_1, \dots, n_{K-1} and activation function $\rho: \mathbb{R} \rightarrow \mathbb{R}$. Let the last affine map $V_K: \mathbb{R}^{n_{K-1}} \rightarrow \mathbb{R}^{2N}$ of Φ , be given by $V_K(s) = W_K s + z$, where $W_K \in \mathbb{R}^{2N \times n_{K-1}}$ is the zero-matrix. Then Ψ is the constant NN which outputs z for all inputs, and hence Φ satisfies (4.1) and it has Lipschitz constant $0 < L$. \square

Proof of Theorem 4.2. Let $r = \text{rank}(A)$ and denote the ordered singular values of A as $\sigma_1(A) \geq \dots \geq \sigma_r(A) > \sigma_{r+1}(A) = \dots = \sigma_{\min\{m, N\}}(A) = 0$. Since all norms on finite dimensional vector spaces are equivalent, let $K_1, K_2 > 0$ be such that

$$\|u\|_{\ell^2} \leq K_1 \|u\| \quad \forall u \in \mathbb{C}^m, \quad \text{and} \quad \|v\| \leq K_2 \|v\|_{\ell^2} \quad \forall v \in \mathbb{C}^N. \quad (\text{B.1})$$

We start by constructing \mathcal{M}_1 . Since $\text{rank}(A) \geq 1$, we can find a vector $\eta \in \mathcal{N}(A)^\perp$ such that $A(\eta + x_{\text{Det}}) \neq 0$ and $\|A\eta\| = \tilde{\epsilon}$, where $\tilde{\epsilon} < \min\{\delta/(4L), \sigma_r(A)\delta/(2K_1K_2)\}$. Fix $x' \in \mathcal{T}$ and let

$$\mathcal{M}_1 = \mathcal{T} \cup \{x' + e^{ni}(\eta + x_{\text{Det}})\}_{n=1}^\infty. \quad (\text{B.2})$$

Observe that $A\mathcal{M}_1 \subset (A\mathcal{T})^\epsilon$, as $\mathcal{T} \subseteq \mathcal{M}_1$ and $\|Ax' - A(x' + e^{ni}(\eta + x_{\text{Det}}))\| = \|A(\eta + x_{\text{Det}})\| < \delta/(2L) \leq \epsilon$ for any $n \in \mathbb{N}$. To get a set \mathcal{M}_1 with finite cardinality simply choose an appropriate subset in (B.2). To create the uncountable family \mathcal{C} , pick any other value for $\tilde{\epsilon} \in (0, \min\{\delta/(4L), \sigma_r(A)\delta/(2K_1K_2)\})$ and repeat the construction.

Next let $n \in \mathbb{N}$ and notice that

$$\begin{aligned} & \|\Psi(A(x' + e^{ni}(\eta + x_{\text{Det}}))) - x'\| \\ & \leq \|\Psi(A(x' + e^{ni}(\eta + x_{\text{Det}}))) - \Psi(Ax')\| + \|\Psi(Ax') - x'\| \\ & \leq L\|A(x' + e^{ni}(\eta + x_{\text{Det}})) - Ax'\| + \delta = \frac{3}{2}\delta. \end{aligned}$$

Next we claim that if $\xi \in \mathcal{N}(A)^\perp$ and $\|A\xi\|_{\ell^2} < c$ for some $c > 0$, then $\|\xi\|_{\ell^2} \leq c/\sigma_r(A)$. To see this, let $u_i \in \mathbb{C}^m$ and $v_i \in \mathbb{C}^N$, $i = 1, \dots, \min\{m, N\}$ denote the (first) left and right singular vectors of A , respectively, corresponding to the singular values $\sigma_i(A)$. Since $\xi \in \mathcal{N}(A)^\perp$ we know that $\xi = \lambda_1 v_1 + \dots + \lambda_r v_r$, for appropriate scalar values λ_i . Moreover, we know that $A\xi = \sigma_1 \lambda_1 u_1 + \dots + \sigma_r \lambda_r u_r$, where $\sigma_i = \sigma_i(A)$. Since the u_i 's and v_i 's are orthonormal, the Pythagorean theorem gives that $\|A\xi\|_{\ell^2}^2 = \sigma_1^2 \lambda_1^2 + \dots + \sigma_r^2 \lambda_r^2$ and $\|\xi\|_{\ell^2}^2 = \lambda_1^2 + \dots + \lambda_r^2$. Since $\sigma_1 \geq \dots \geq \sigma_r$ and $\|A\xi\|_{\ell^2} \leq c$, it is clear that $\|\xi\|_{\ell^2}$ is maximized for $\lambda_1 = \dots = \lambda_{r-1} = 0$ and $\lambda_r = c/\sigma_r$, in which case $\|\xi\|_{\ell^2} = c/\sigma_r$. This proves the claim.

Now, since $\eta \in \mathcal{N}(A)^\perp$ and $\|A\eta\| = \tilde{\epsilon}$, we know from (B.1) that $\|A\eta\|_{\ell^2} \leq K_1\|A\eta\| = K_1\tilde{\epsilon} < \sigma_r(A)\delta/(2K_2)$. By the above claim and (B.1) we deduce that $\|\eta\| \leq K_2\|\eta\|_{\ell^2} \leq \delta/2$.

Next let $\lambda = -e^{ni}$. Then

$$\begin{aligned} & \|\Psi(A(x' + e^{ni}(\eta + x_{\text{Det}}))) - (x' + e^{ni}(\eta + x_{\text{Det}}) + \lambda x_{\text{Det}})\| \\ & \leq \|\Psi(A(x' + e^{ni}(\eta + x_{\text{Det}}))) - x'\| + \|e^{ni}\eta\| \leq 2\delta. \end{aligned} \tag{B.3}$$

By assumption $\mathbb{P}_{X \sim \mathcal{D}}(X \in \mathcal{M}_1 \setminus \mathcal{T}) \geq 1 - q$. Now, since any $X \in \mathcal{M}_1 \setminus \mathcal{T}$ is of the form $X = x' + e^{ni}(\eta + x_{\text{Det}})$ the result follows from (B.3).

Next we show (ii) for our choice of $\mathcal{M}_1 \in \mathcal{C}$. Recall that by ‘‘algorithm’’ we mean a Blum-Shub-Smale (BSS) machine [26] (see [25] for an overview). In particular, this means that the algorithm can perform arithmetic operations with real numbers, and check if two real numbers are equal. We describe the algorithm $\Gamma(y)$, taking an input $y \in \mathcal{AM}_1$ and yielding a NN $\Phi_y: \mathbb{C}^m \rightarrow \mathbb{C}^N$ as output in the following pseudo-code:

```

1: for all  $x \in \mathcal{T}$  do
2:   if  $y = Ax$  then
3:      $\Phi_y \leftarrow \Psi$  and return  $\Phi_y$ ;
4:   end if
5: end for
6: set  $l = 1$  and  $u = A(\eta + x_{\text{Det}})$ ;
7: while  $u[l] = 0$  do
8:    $l \leftarrow l + 1$ ;
9: end while
10: set  $c = (y[l] - (Ax')[l])/u[l]$ ;
11: let  $\Phi_y$  be a such that  $\Phi_y(y) = x' + c(\eta + x_{\text{Det}})$  and return  $\Phi_y$ .
```

A few comments are in order. The set \mathcal{T} is finite, and the first for loop will, therefore, either terminate or return the desired NN. The while loop finds an index $l \in \{1, \dots, m\}$ such that $A(\eta + x_{\text{Det}})[l] = u[l] \neq 0$. Such an index exists since $A(\eta + x_{\text{Det}}) \neq 0$ by construction. Next, notice that if $x \in \mathcal{M}_1 \setminus \mathcal{T}$, then $x = x' + e^{in}(\eta + x_{\text{Det}})$ for some $n \in \mathbb{N}$. Hence, if $y = Ax$, then

$$\frac{(y - Ax')[l]}{u[l]} = \frac{(A(x' + e^{in}(\eta + x_{\text{Det}})) - Ax')[l]}{(A(\eta + x_{\text{Det}}))[l]} = e^{in} = c.$$

Finally, we choose $\Phi_y: \mathbb{C}^m \rightarrow \mathbb{C}^N$ as a NN where all the weights and biases are zero, except the bias in the final layer, which is equal to $x' + c(\eta + x_{\text{Det}})$. Since $c = e^{in}$, this means that $\Phi_y(y) = x' + c(\eta + x_{\text{Det}})$ will identify the vector $x \in \mathcal{M}_1 \setminus \mathcal{T}$. \square

B.2 Proofs of Theorems 4.4, 4.5 and 4.6

Proof of Theorem 4.4. Consider part (i). Let $y = Ax$ and note that $\|Ax - Ax'\| \leq \eta \leq \epsilon$. We apply this fact, together with the reverse triangle inequality and the assumption (4.2) to get

that

$$\begin{aligned} L^\epsilon(\Psi, y) &= \sup_{\substack{e \in \mathbb{C}^m \\ \|e\| \leq \epsilon}} \frac{\|\Psi(y) - \Psi(y+e)\|}{\|e\|} \geq \frac{1}{\eta} \|\Psi(Ax) - \Psi(Ax')\| \\ &\geq \frac{1}{\eta} (\|x'' - x\| - \|\Psi(Ax) - x\| - \|\Psi(Ax') - x''\|) > \frac{1}{\eta} (\|x'' - x\| - 2\eta). \end{aligned} \quad (\text{B.4})$$

The continuity of Ψ and the strict inequality in (B.4) now implies that there exists a closed non-empty ball $\mathcal{B} \subset \mathbb{C}^m$ centred at $y = Ax$ such that,

$$L^\epsilon(\Psi, \tilde{y}) \geq \frac{1}{\eta} (\|x - x''\| - 2\eta).$$

for all $\tilde{y} \in \mathcal{B}$. This gives the result.

For part (ii), let $z = x'' - x$ and $e = Ax' - Ax$. Clearly, $\|z\| \geq \|x - x''\|$ and $\|e\| \leq \eta$. Moreover, we have that

$$\|\Psi(Ax + e) - (x + z)\| = \|\Psi(Ax') - x''\| < \eta.$$

The result once more follows from continuity of Ψ . \square

Proof of Theorem 4.5. Consider part (i). Let $e = Ax' - Ax$ and notice by using the reverse triangle inequality and (4.2), we have that $\|\Psi(Ax + e) - \Psi(Ax)\| > \|x - x''\| - 2\eta$. Using the continuity of Ψ , we can find a closed ball $\mathcal{B}_x \subset \mathbb{C}^N$ centered at x and an $\epsilon > 0$, such that

$$\|\Psi(A\tilde{x} + \tilde{e}) - \Psi(A\tilde{x})\| \geq \|x - x''\| - 2\eta \quad \forall \tilde{e} \in \mathcal{B}(e, \epsilon), \forall \tilde{x} \in \mathcal{B}_x.$$

Now, by assumption E has a probability density function $g: \mathbb{C}^m \rightarrow \mathbb{R}_{>0}$ which is strictly positive. Thus,

$$\mathbb{P}(\|\Psi(A\tilde{x} + E) - \Psi(A\tilde{x})\| \geq \|x - x''\| - 2\eta) \geq \mathbb{P}(E \in \mathcal{B}(e, \epsilon)) = \int_{\mathcal{B}(e, \epsilon)} g \, d\mu > 0,$$

for all $\tilde{x} \in \mathcal{B}_x$, since g is strictly positive.

For the second part of the statement note that $\|e\| \leq \eta$ by (4.3). Furthermore, let $I \in \mathbb{C}^{m \times m}$ denote the identity matrix, $\sigma > 0$ and let $E \sim \mathcal{CN}(e, \sigma^2 I)$. Then

$$\begin{aligned} \mathbb{P}(E \in \mathcal{B}(e, \epsilon)) &= \frac{1}{(\pi\sigma^2)^m} \int_{\mathcal{B}(e, \epsilon)} \exp\left(-\frac{1}{\sigma^2} \|t - e\|_{\ell^2}^2\right) dt \\ &= \frac{1}{\pi^m} \int_{\mathcal{B}(0, \epsilon/\sigma)} \exp(-\|u\|_{\ell^2}^2) du, \end{aligned} \quad (\text{B.5})$$

where we in the second equality applied the change of variables $t = \sigma u + e$. From (B.5), we observe that $\mathbb{P}(E \in \mathcal{B}(e, \epsilon)) \rightarrow 1$ as $\sigma \rightarrow 0$. Thus, for any choice of $\delta \in (0, 1)$ we can find a σ such that (4.6) holds with $c = 1 - \delta$, as required.

Part (ii) is proved analogously to part (i) from Theorem 4.4, combined with the arguments above. \square

Proof of Theorem 4.6. First observe that $AA^* = P_\Omega U U^* P_\Omega^* = I$, where I is the identity matrix, since U is unitary and $P_\Omega \in \mathbb{C}^{m \times N}$ is a projection. It follows, that $\|Au\|_{\ell^2} \leq \|u\|_{\ell^2}$ for all $u \in \mathbb{C}^N$ and $\|A^*v\|_{\ell^2} = \|v\|_{\ell^2}$ for all $v \in \mathbb{C}^m$. Moreover, it implies that $A\tilde{x}' - Ax \in \mathcal{B}(Ax' - Ax, \delta)$ if $\tilde{x}' \in \mathcal{B}(x', \delta)$. Moreover, the converse is also true. That is, if $\tilde{e} \in \mathcal{B}(Ax' - Ax, \delta)$ then there exists a $\tilde{x}' \in \mathcal{B}(x', \delta)$ such that $A\tilde{x}' - Ax = \tilde{e}$. Indeed, by assumption $\tilde{e} = Ax' - Ax + v$, where $\|v\|_{\ell^2} \leq \delta$, but then we have that $\tilde{x}' = x' + A^*v \in \mathcal{B}(x', \delta)$.

This means that we for every $\tilde{e} \in \mathcal{B}(Ax' - Ax, \delta)$ we can find a corresponding $\tilde{x} \in \mathcal{B}(x', \delta)$ such that

$$\|\Psi(Ax + \tilde{e}) - \Psi(Ax)\|_{\ell^2} = \|\Psi(A\tilde{x}') - \Psi(Ax)\|_{\ell^2} > \|x - x''\|_{\ell^2} - 2\eta,$$

where the last inequality follows from the assumption $\|A\tilde{x}' - x''\|_{\ell^2} < \eta$. Moreover, since for every $\tilde{x} \in \mathcal{B}(x', \delta)$ we can find a x'' satisfying the above inequality, it is clear that by taking the infimum over all possible such x'' we obtain a lower bound for any choice of $\tilde{e} \in \mathcal{B}(Ax' - Ax, \delta)$, i.e.,

$$\|\Psi(Ax + \tilde{e}) - \Psi(Ax)\|_{\ell^2} \geq \inf_{x'' \in \mathcal{S}} \|x - x''\|_{\ell^2} - 2\eta \quad \text{for all } \tilde{e} \in \mathcal{B}(Ax' - Ax, \delta). \quad (\text{B.6})$$

Next consider $E \sim \mathbb{CN}(\xi, \sigma^2 I)$ and observe that

$$\begin{aligned} & \mathbb{P} \left(\|\Psi(Ax + E) - \Psi(Ax)\|_{\ell^2} \geq \inf_{x'' \in \mathcal{S}} \|x - x''\|_{\ell^2} - 2\eta \right) \\ & \geq \mathbb{P}(E \in \mathcal{B}(Ax' - Ax, \delta)) = (\pi\sigma^2)^{-m} \int_{\mathcal{B}} \exp \left(-\frac{1}{\sigma^2} \|t - \xi\|_{\ell^2}^2 \right) dt. \end{aligned} \quad (\text{B.7})$$

This establishes (4.9).

We proceed by considering the claim of the existence of a variance σ_0 maximizing (4.9). Let $\mu(\mathcal{B})$ denote the Lebesgue measure of \mathcal{B} and let $\gamma = Ax' - Ax - \xi$. Now, observe that for $t \in \mathcal{B} = \mathcal{B}(Ax' - Ax, \delta)$, we have that

$$\|\gamma\|_{\ell^2} - \delta \leq \|t - \xi\|_{\ell^2} \leq \|\gamma\|_{\ell^2} + \delta. \quad (\text{B.8})$$

We claim that the mapping

$$\sigma \mapsto (\pi\sigma^2)^{-m} \int_{\mathcal{B}} \exp \left(-\frac{1}{\sigma^2} \|t - \xi\|_{\ell^2}^2 \right) dt, \quad \text{for } \sigma > 0 \quad (\text{B.9})$$

has a maximum. To see this, observe that

$$(\pi\sigma^2)^{-m} \int_{\mathcal{B}} \exp \left(-\frac{1}{\sigma^2} \|t - \xi\|_{\ell^2}^2 \right) dt \leq (\pi\sigma^2)^{-m} \mu(\mathcal{B}) \exp(-\sigma^{-2}(\|\gamma\|_{\ell^2} - \delta)^2) \quad (\text{B.10})$$

and notice that the upper bound in (B.10) tends to zero when $\sigma \rightarrow 0$ and when $\sigma \rightarrow \infty$. This means that we can restrict the domain of the mapping in (B.9) to a closed interval, when searching for the maximum. The existence of the maximum then follows by the continuity of (B.9) and the Extreme Value Theorem.

Next, observe that the derivative of (B.9) is given by

$$\begin{aligned} & \frac{d}{d\sigma} \left[(\pi\sigma^2)^{-m} \int_{\mathcal{B}} \exp \left(-\frac{1}{\sigma^2} \|t - \xi\|_{\ell^2}^2 \right) dt \right] \\ & = \frac{1}{\pi^m \sigma^{2m+1}} \int_{\mathcal{B}} \exp \left(-\frac{1}{\sigma^2} \|t - \xi\|_{\ell^2}^2 \right) \left(\frac{2\|t - \xi\|_{\ell^2}^2}{\sigma^2} - 2m \right) dt \end{aligned} \quad (\text{B.11})$$

Now, by setting (B.11) equal to zero, and rearranging the terms we get an expression for the σ_0 maximizing (B.9),

$$\sigma_0^2 = \frac{\int_{\mathcal{B}} \exp \left(-\frac{1}{\sigma_0^2} \|t - \xi\|_{\ell^2}^2 \right) \|t - \xi\|_{\ell^2}^2 dt}{m \int_{\mathcal{B}} \exp \left(-\frac{1}{\sigma_0^2} \|t - \xi\|_{\ell^2}^2 \right) dt}. \quad (\text{B.12})$$

Using (B.8) we see that

$$\sigma_0^2 \leq \frac{\mu(\mathcal{B}) \exp(-\sigma_0^{-2}(\|\gamma\|_{\ell^2} - \delta)^2) (\|\gamma\|_{\ell^2} + \delta)^2}{m \mu(\mathcal{B}) \exp(-\sigma_0^{-2}(\|\gamma\|_{\ell^2} + \delta)^2)} = \frac{\exp(4\sigma_0^{-2}\|\gamma\|_{\ell^2}\delta) (\|\gamma\|_{\ell^2} + \delta)^2}{m}. \quad (\text{B.13})$$

Rearranging the terms yields

$$0 \leq \sigma_0^2 \exp(-4\sigma_0^{-2}\|\gamma\|_{\ell^2}\delta) \leq \frac{(\|\gamma\|_{\ell^2} + \delta)^2}{m}$$

which implies that $\sigma_0 \rightarrow 0$ when $m \rightarrow \infty$.

By assumption $\|Ax' - Ax - \xi\|_{\ell^2} < \delta$. Hence, we must have $\mathcal{B}(\xi, \delta') \subseteq \mathcal{B}$ for some $\delta' \leq \delta$. Next, apply the change of variables $t = \sigma u + \xi$ so that the integral in (4.9) can be bounded below by

$$\pi^{-m} \int_{\mathcal{B}'} \exp(-\|u\|_{\ell^2}^2) du,$$

where $\mathcal{B}' = \mathcal{B}(0, \delta'/\sigma)$. Recall that $\pi^{-m} \int_{\mathbb{C}^m} \exp(-\|u\|_{\ell^2}^2) du = 1$. Hence, for each m , let $\sigma = \sigma(m)$ be sufficiently small so that this integral is $\geq 1 - 1/m$. The result now follows. \square

B.3 Proof of Theorem 4.9

Proof of Theorem 4.9. We begin with the proof of (ii). First, let $\{x_1, \dots, x_K\}$ be K distinct elements in $\mathcal{N}(A)^\perp$ such that $\|x_1\| = 1/2$ and $0 < \|x_j\| \leq 1$. Note that we can do this since, by assumption, $\text{rank}(A) \geq 1$. Now, since $\text{rank}(A) < N$, we can choose a $z_1 \in \mathcal{N}(A)$ with $\|z_1\| = 1/2$. Let $\mathcal{M}_1 = \{x_1 + z_1, x_1, \dots, x_K\}$ and observe that $\mathcal{M}_1 \subset \mathcal{B}$. We argue by contradiction and suppose that there exists a (possibly multivalued) map $\Psi : \mathcal{M}_2 \rightrightarrows \mathbb{C}^N$ with

$$d^H(\Psi(Ax), x) \leq \delta, \quad \forall x \in \mathcal{M}_1. \quad (\text{B.14})$$

In particular, $d^H(\Psi(Ax_1), x_1) \leq \delta$. However, since $z_1 \in \mathcal{N}(A)$, we have $\Psi(A(x_1 + z_1)) = \Psi(Ax_1)$ and therefore $d^H(\Psi(A(x_1 + z_1)), x_1 + z_1) \geq \|z_1\| - \delta \geq 1/2 - 1/5 > \delta$, which contradicts (B.14). Since K is arbitrary, we get the result. In order to get uncountably many different \mathcal{M}_1 's, as mentioned in the statement of the theorem, one can simply multiply the original choice of \mathcal{M}_1 by complex numbers of modulus 1.

To prove (i) we use the setup from the proof of (ii). Indeed, let \mathcal{M}_1 be as defined previously, and set $\mathcal{T} = \{x_1, \dots, x_K\}$. Define the map $\psi_0 : \mathcal{M}_2 \rightarrow \mathbb{C}^N$ by

$$\psi_0(y) = \begin{cases} x_1 + \frac{1}{2}z_1 & \text{if } y = Ax_1 \\ x_1 + \frac{1}{2}z_1 & \text{if } y = A(x_1 + z_1) \\ x_j & \text{otherwise} \end{cases}. \quad (\text{B.15})$$

Then, by (B.15),

$$\begin{aligned} c_{\text{opt}}(A, \mathcal{M}_1) &= \inf_{\varphi : \mathcal{M}_2 \rightrightarrows \mathcal{M}_1} \sup_{x \in \mathcal{M}_1} d_1^H(\varphi(Ax), x) \leq \sup_{x \in \mathcal{M}_1} \|\psi_0(Ax) - x\| \\ &\leq \sup_{j \geq 1} \|\psi_0(Ax_j) - x_j\| \vee \|\psi_0(A(x_1 + z_1)) - (x_1 + z_1)\| = \frac{1}{4}, \end{aligned} \quad (\text{B.16})$$

where $a \vee b$ denotes the standard maximum of real numbers a, b . However, for any mapping $\Psi : \mathcal{M}_2 \rightrightarrows \mathbb{C}^N$ with

$$d^H(\Psi(Ax_j), x_j) \leq \delta, \quad \forall j = 1, \dots, K, \quad (\text{B.17})$$

we have that

$$\begin{aligned} \sup_{x \in \mathcal{M}_1} d^H(\Psi(Ax), x) &\geq d^H(\Psi(A(x_1 + z_1)), x_1 + z_1) \\ &= d^H(\Psi(Ax_1), x_1 + z_1) \geq \|z_1\| - d^H(\Psi(Ax_1), x_1) \geq \frac{1}{2} - \frac{1}{5} = \frac{3}{10} > \frac{1}{4}. \end{aligned}$$

Thus, by (B.16), it follows that Ψ is not an optimal map. Furthermore, it is clear that no family of maps satisfying (B.17) can be approximately optimal. \square

B.4 Proof of Theorem 4.12

Proof Theorem 4.12. We first define $\Omega, \tilde{\Omega}, \mathcal{M}_1, \mathcal{T}$ and $\tilde{\mathcal{T}}$. Let $\tilde{\Omega} \subset \{1, \dots, N\}$ with $2 \leq |\tilde{\Omega}| \leq N - 2$ and note that there are $2^N - 2N - 2$ different choices of $\tilde{\Omega}$. Also, let $\Omega = \tilde{\Omega} \cup \{j\}$ where $j \notin \tilde{\Omega}$, and notice that $|\Omega| < N$ since $|\tilde{\Omega}| \leq N - 2$.

Next, choose $i \in \tilde{\Omega}$ and let $\hat{x} \in \mathcal{N}(P_{\{i\}}U)^\perp$ be non-zero, where $P_{\{i\}}$ denotes the projection onto the i th coordinate. If M is finite, choose a set $\mathcal{K} \subset \mathcal{N}(P_{\tilde{\Omega} \setminus \{i\}}U)^\perp \setminus \{0\}$ of size $M-1$, and if M is infinite, choose \mathcal{K} to be countable. Note that this is possible since $|\tilde{\Omega}| \geq 2$. Let $\mathcal{M}_1 = \{\hat{x}\} \cup \mathcal{K}$, and note that by multiplying the elements of \mathcal{M}_1 by a real number we get uncountably many different choices of \mathcal{M}_1 . For ease of notation let $\mathcal{M}_2 = A(\mathcal{M}_1)$ and $\tilde{\mathcal{M}}_2 = \tilde{A}(\mathcal{M}_1)$.

Let $\hat{y} = \tilde{A}\hat{x}$ and note that there is a $k \in \{1, \dots, m-1\}$, such that $\hat{y}_k \neq 0$, whereas $P_{\{k\}}^\perp \hat{y} = 0$. Likewise, if $x \in \mathcal{K}$ and $y = \tilde{A}x$, then $y_i = 0$ and $P_{\{k\}}^\perp y \neq 0$. Finally, let $\tilde{\mathcal{T}} \subset \tilde{\mathcal{M}}_2 \times \mathcal{M}_1$ be any finite, non-zero collection such that $(\hat{y}, \hat{x}) \in \tilde{\mathcal{T}}$ and let $\mathcal{T} \subset \mathcal{M}_2 \times \mathcal{M}_1$ be any finite, non-empty set, not containing zero.

Next let \tilde{A}^\dagger denotes the pseudoinverse of $\tilde{A} = P_{\tilde{\Omega}}U$, and note that

$$\tilde{A}^\dagger y = x \text{ if } y = \tilde{A}x, \quad x \in \mathcal{M}_1, \quad (\text{B.18})$$

since $\mathcal{M}_1 \subset \mathcal{N}(\tilde{A})^\perp$. This fact will be crucial later in the proof.

For convenience, we denote all NNs in what follows as taking complex input and producing complex output, with this being understood in the sense discussed after (3.1) in the main paper. Consider the L -layer ReLU NN $\tilde{\Psi} : \mathbb{C}^{|\tilde{\Omega}|} \rightarrow \mathbb{C}^N$ defined by

$$\tilde{\Psi}(y) = \tilde{A}^\dagger W_2 \rho(\dots \rho(W_1 W_2 \rho(W_1 W_2 \rho(W_1 y))))), \quad (\text{B.19})$$

where

$$W_1 = (1, -1)^\top \otimes I_{|\tilde{\Omega}|}, \quad W_2 = (1, -1) \otimes I_{|\tilde{\Omega}|}, \quad (\text{B.20})$$

where I_d denotes the $d \times d$ identity matrix and \otimes denotes the Kronecker product. Observe that

$$W_2 \rho(W_1 \tilde{y}) = W_2 \begin{pmatrix} \rho(\tilde{y}) \\ \rho(-\tilde{y}) \end{pmatrix} = \rho(\tilde{y}) - \rho(-\tilde{y}) = \tilde{y},$$

where the last equality is due to the fact that ρ is the ReLU activation function. Hence, for every $(\tilde{y} = \tilde{A}\tilde{x}, \tilde{x}) \in \tilde{\mathcal{M}}_2 \times \mathcal{M}_1$, we have

$$\tilde{\Psi}(\tilde{y}) = \tilde{A}^\dagger W_2 \rho(\dots \rho(W_1 W_2 \rho(W_1 W_2 \rho(W_1 \tilde{y})))) = \tilde{A}^\dagger \tilde{y} = \tilde{x}, \quad (\text{B.21})$$

Also, recalling that $\mathbf{n} = (m, n_1, \dots, n_{L-1}, N)$, $m = \max\{|\Omega|, |\tilde{\Omega}|\}$ and the assumption that $n_j \geq 2m$, it is clear that by suitably padding W_j with zeros we can without loss of generality assume that $\tilde{\Psi} \in \mathcal{N}_{\mathbf{n}}$. Hence, by setting λ_{opt} to zero, and using (B.21) we have that

$$\max_{J \in \mathcal{K}} \frac{1}{|\tilde{\mathcal{T}}|} \sum_{(\tilde{y}, \tilde{x}) \in \tilde{\mathcal{T}}} \frac{1}{2} \|\tilde{x} - \tilde{\Psi}(\tilde{y})\|^2 + \lambda_{\text{opt}} J(\tilde{\Psi}, \tilde{\mathcal{T}}) = 0. \quad (\text{B.22})$$

We use this choice of λ_{opt} throughout the argument. We first claim that λ_{opt} is optimal for $\{\tilde{A}, \mathcal{M}_1\}, \mathcal{N}, \mathcal{K}, \tilde{\mathcal{T}}\}$. Since (B.22) implies that $\tilde{\Psi}$ is a minimizer of (4.15) for $\lambda = \lambda_{\text{opt}}$ we only need to show that $\tilde{\Psi}$ is an optimal map for $\{\tilde{A}, \mathcal{M}_1\}$. To see this, we use (B.21) to obtain

$$c_{\text{opt}}(\tilde{A}, \mathcal{M}_1) = \inf_{\Psi: \tilde{\mathcal{M}}_2 \rightarrow \mathbb{C}^N} \sup_{x \in \mathcal{M}_1} d^H(\Psi(\tilde{A}x), x) \leq \sup_{x \in \mathcal{M}_1} d^H(\tilde{\Psi}(\tilde{A}x), x) = 0. \quad (\text{B.23})$$

Hence claim that λ_{opt} is optimal for $\{\tilde{A}, \mathcal{M}_1\}, \mathcal{N}, \mathcal{K}, \tilde{\mathcal{T}}\}$ holds. That λ_{opt} also is optimal for $\{\tilde{A}, \mathcal{M}_1\}, \mathcal{N}, \mathcal{T}\}$, will be shown when we consider part (ii).

We now define \mathcal{S} . Note that $\mathcal{N}(\tilde{A}) \cap (\mathcal{N}(A))^\perp$ is non-trivial by our choice of Ω . We choose a nonzero $x \in \mathcal{N}(\tilde{A}) \cap (\mathcal{N}(A))^\perp$ and let $z = \hat{x} + x$ where \hat{x} is as chosen above. We then define \mathcal{S} as any uncountable collection of nonzero multiples of z .

We are now ready to show (i). Note that it is enough to show that λ_{opt} is no longer optimal if we add or replace a specific element of $\tilde{\mathcal{T}}$ with an element from \mathcal{S} . First, suppose that we replace $(\hat{y}, \hat{x}) \in \tilde{\mathcal{T}}$ by $(\hat{y}, \hat{x} + x)$. Define the NN $\Phi \in \mathcal{N}$ by

$$\Phi(y) = T \rho(\dots \rho(W_1 W_2 \rho(W_1 W_2 \rho(W_1 y))))), \quad (\text{B.24})$$

where W_1 and W_2 are as in (B.20) and

$$T = C((1, -1) \otimes I_{|\tilde{\Omega}|}), \quad C = \tilde{A}^\dagger P_{\{k\}}^\perp + (\frac{1}{e_k^\top \hat{y}}(\hat{x} + x) \otimes e_k^\top).$$

where k is such that $\hat{y}_k \neq 0$. Observe that $\Phi(\tilde{y}) = \tilde{\Psi}(\tilde{y}) = \tilde{x}$ for $(\tilde{y}, \tilde{x}) \in \tilde{\mathcal{T}}$ with $\tilde{y}_k = 0$. Moreover

$$\Phi(\hat{y}) = \left(\tilde{A}^\dagger P_{\{k\}}^\perp + \left(\frac{1}{\hat{y}_k}(\hat{x} + x) \otimes e_k^\top \right) \right) \hat{y} = \hat{x} + x,$$

for $(\hat{y}, \hat{x} + x) \in \tilde{\mathcal{T}}$. Hence, the objective function in (4.15) is zero at Φ whenever $\lambda = \lambda_{\text{opt}}$. Thus, every

$$\hat{\Psi} \in \underset{\varphi \in \mathcal{NN}}{\text{argmin}} \max_{J \in \mathcal{K}} \frac{1}{|\tilde{\mathcal{T}}|} \sum_{(\tilde{y}, \tilde{x}) \in \tilde{\mathcal{T}}} \frac{1}{2} \|\tilde{x} - \varphi(\tilde{y})\|^2 + \lambda_{\text{opt}} J(\varphi, \tilde{\mathcal{T}}) \quad (\text{B.25})$$

must satisfy $\hat{\Psi}(\hat{y}) = \hat{x} + x$, which means that

$$\sup_{x \in \mathcal{M}_1} d^H(\hat{\Psi}(\tilde{A}x), x) \neq 0.$$

It follows from (B.23) that $\hat{\Psi}$ is not an optimal map. Hence λ_{opt} is no longer optimal for $\{\tilde{A}, \mathcal{M}_1\}, \mathcal{NN}, \mathcal{K}, \tilde{\mathcal{T}}\}$.

Now consider the case where $(\hat{y}, \hat{x} + x)$ is added to $\tilde{\mathcal{T}}$. Let $\tilde{\Phi}$ be the NN defined by (B.24) with

$$T = D((1, -1) \otimes I_{|\tilde{\Omega}|}), \quad D = \tilde{A}^\dagger P_{\{k\}}^\perp + (\frac{1}{e_k^\top \hat{y}}(\hat{x} + \frac{1}{2}x) \otimes e_k^\top).$$

Observe that $\tilde{\Phi}(\tilde{y}) = \tilde{x}$ for $(\tilde{y}, \tilde{x}) \in \tilde{\mathcal{T}}$ with $\tilde{y}_k = 0$ and

$$\tilde{\Phi}(\hat{y}) = \left(\tilde{A}^\dagger P_{\{k\}}^\perp + (\frac{1}{\hat{y}_k}(\hat{x} + \frac{1}{2}x) \otimes e_k^\top) \right) \hat{y} = \hat{x} + \frac{1}{2}x,$$

for $(\hat{y}, \hat{x} + x), (\hat{y}, \hat{x}) \in \tilde{\mathcal{T}}$. Hence

$$\frac{1}{|\tilde{\mathcal{T}}|} \sum_{(\tilde{y}, \tilde{x}) \in \tilde{\mathcal{T}}} \frac{1}{2} \|\tilde{x} - \tilde{\Phi}(\tilde{y})\|^2 + \lambda_{\text{opt}} J(\tilde{\Phi}) = \frac{1}{2|\tilde{\mathcal{T}}|} \|\frac{1}{2}x\|^2,$$

and therefore every minimizer φ of (B.25) satisfies

$$\max_{J \in \mathcal{K}} \frac{1}{|\tilde{\mathcal{T}}|} \sum_{(\tilde{y}, \tilde{x}) \in \tilde{\mathcal{T}}} \frac{1}{2} \|\tilde{x} - \varphi(\tilde{y})\|^2 + \lambda_{\text{opt}} J(\varphi, \tilde{\mathcal{T}}) \leq \frac{1}{8|\tilde{\mathcal{T}}|} \|x\|^2. \quad (\text{B.26})$$

However, by (B.23), every optimal map Ψ for $(\tilde{A}, \mathcal{M}_1)$ satisfies

$$\sup_{x \in \mathcal{M}_1} d^H(\Psi(\tilde{A}x), x) = 0.$$

Thus,

$$\frac{1}{|\tilde{\mathcal{T}}|} \sum_{(\tilde{y}, \tilde{x}) \in \tilde{\mathcal{T}}} \frac{1}{2} \|\tilde{x} - \Psi(\tilde{y})\|^2 = \frac{1}{2|\tilde{\mathcal{T}}|} \|x\|^2,$$

and therefore, by (B.26), no minimizer φ of (B.25) can be an optimal map for $\{\tilde{A}, \mathcal{M}_1\}$. Hence λ_{opt} is not optimal for $\{\tilde{A}, \mathcal{M}_1, \mathcal{NN}, \mathcal{K}, \tilde{\mathcal{T}}\}$.

Now consider part (ii). Let $\mathcal{V} \subset \mathcal{M}_1 \cup \mathcal{S}$ be any finite non-empty set, and let

$$\mathcal{T} = \{(Ax, x) : x \in \mathcal{V}\}.$$

We shall prove that λ_{opt} is optimal for $\{\{A, \mathcal{N}(A)^\perp\} \mathcal{NN}, \mathcal{K}, \mathcal{T}\}$ for any such \mathcal{T} . Note that this is a stronger statement than in the theorem, as

$$\mathcal{M}_1 \cup \mathcal{S} \subset \mathcal{N}(A)^\perp.$$

From (B.23) it is clear that $y \mapsto A^\dagger y$ is an optimal map for $\{A, \mathcal{N}(A)^\perp\}$. Using the NN $\tilde{\Psi}$ from (B.21), where \tilde{A}^\dagger is replaced by A^\dagger in the last layer, it is clear that $\tilde{\Psi}$ is an optimal map, and a minimizer of (B.25) for λ_{opt} when we replace $\tilde{\mathcal{T}}$ by \mathcal{T} . Thus λ_{opt} is optimal for $\{\{A, \mathcal{N}(A)^\perp\}, \mathcal{NN}, \mathcal{K}, \mathcal{T}\}$. \square

References

- [1] B. Adcock, S. Brugiapaglia, N. Dexter, and S. Moraga. Deep neural networks are effective at learning high-dimensional Hilbert-valued functions from limited data. In J. Bruna, J. S. Hesthaven, and L. Zdeborová, editors, *Proceedings of The Second Annual Conference on Mathematical and Scientific Machine Learning*, volume 145 of *Proc. Mach. Learn. Res. (PMLR)*, pages 1–36. PMLR, 2021.
- [2] B. Adcock and N. Dexter. The gap between theory and practice in function approximation with deep neural networks. *SIAM J. Math. Data Sci.*, 3(2):624–655, 2021.
- [3] B. Adcock and A. C. Hansen. *Compressive Imaging: Structure, Sampling, Learning*. Cambridge University Press, Cambridge, UK, 2021.
- [4] J. Adler and O. Öktem. Solving ill-posed inverse problems using iterative deep neural networks. *Inverse Problems*, 33(12):124007, 2017.
- [5] J. Adler and O. Öktem. Learned primal-dual reconstruction. *IEEE Trans. Med. Imaging*, 37(6):1322–1332, 2018.
- [6] R. Ahmad, C. A. Bouman, G. T. Buzzard, S. Chan, S. Liu, E. T. Reehorst, and P. Schniter. Plug-and-play methods for magnetic resonance imaging: Using denoisers for image recovery. *IEEE Signal. Process. Mag.*, 37(1):105–116, 2020.
- [7] R. Alaifari, G. S. Alberti, and T. Gauksson. Localized adversarial artifacts for compressed sensing MRI. *arXiv:2206.05289*, 2022.
- [8] H. H. Andersen, M. Højbjerg, D. Sørensen, and P. S. Eriksen. *Linear and graphical models: for the multivariate complex normal distribution*, volume 101. Springer Science & Business Media, 1995.
- [9] V. Antun, N. M. Gottschling, F. Renna, K. M. Haug, B. Adcock, and A. C. Hansen. On non-robustness, hallucinations and unpredictability in AI for imaging. *Preprint*, 2022.
- [10] V. Antun, F. Renna, C. Poon, B. Adcock, and A. C. Hansen. On instabilities of deep learning in image reconstruction and the potential costs of AI. *Proc. Natl. Acad. Sci. USA*, 117(48):30088–30095, 2020.
- [11] S. Arridge, P. Maass, O. Öktem, and C.-B. Schönlieb. Solving inverse problems using data-driven models. *Acta Numer.*, 28:1–174, 2019.
- [12] N. Avidan and M. Freiman. Physically-primed deep-neural-networks for generalized undersampled MRI reconstruction. *arXiv:2209.00462*, 2022.
- [13] D. O. Bague, J. Leuschner, and M. Schmidt. Computed tomography reconstruction using deep image prior and learned reconstruction methods. *Inverse Problems*, 36(9):094004, 2020.
- [14] R. Barbano, C. Zhang, S. Arridge, and B. Jin. Quantifying model uncertainty in inverse problems via bayesian deep gradient descent. In *2020 25th International Conference on Pattern Recognition (ICPR)*, pages 1392–1399. IEEE, 2021.
- [15] H. H. Barrett and K. J. Myers. *Foundations of image science*. John Wiley & Sons, 2013.
- [16] A. Bastounis, A. C. Hansen, and V. Vlačić. The extended Smale’s 9th problem – On computational barriers and paradoxes in estimation, regularisation, computer-assisted proofs and learning. *arXiv:2110.15734*, 2021.
- [17] A. Bastounis, A. C. Hansen, and V. Vlačić. The mathematics of adversarial attacks in AI – Why deep learning is unstable despite the existence of stable neural networks. *arXiv:2109.06098*, 2021.
- [18] A. Beck. *First-order methods in optimization*. SIAM, 2017.
- [19] C. Belthangady and L. A. Royer. Applications, promises, and pitfalls of deep learning for fluorescence image reconstruction. *Nature methods*, 16(12):1215–1225, 2019.
- [20] H. Ben Yedder, B. Cardoen, and G. Hamarneh. Deep learning for biomedical image reconstruction: A survey. *Artificial intelligence review*, 54(1):215–251, 2021.
- [21] A. Berk, S. Brugiapaglia, B. Joshi, Y. Plan, M. Scotte, and O. Yilmaz. A coherence parameter characterizing generative compressed sensing with Fourier measurements. *arXiv:2207.09340*, 2022.
- [22] S. Bhadra, V. A. Kelkar, F. J. Brooks, and M. A. Anastasio. On hallucinations in tomographic image reconstruction. *IEEE T. Med. Imaging*, 40(11):3249–3260, 2021.

- [23] K. Bhattacharya, N. Hosseini, B. Kovachki, and A. Stuart. Model reduction and neural networks for parametric PDEs. *J. Comput. Math.*, 7:121–157, 2021.
- [24] P. Binev, A. Bonito, R. DeVore, and G. Petrova. Optimal learning. *arXiv:2203.15994*, 2022.
- [25] L. Blum, F. Cucker, M. Shub, and S. Smale. *Complexity and Real Computation*. Springer-Verlag New York, Inc., Secaucus, NJ, USA, 1998.
- [26] L. Blum, M. Shub, and S. Smale. On a theory of computation and complexity over the real numbers: NP-completeness, recursive functions and universal machines. *American Mathematical Society. Bulletin.*, 21(1):1–46, 1989.
- [27] H. Boche, A. Fono, and G. Kutyniok. Limitations of deep learning for inverse problems on digital hardware. *arXiv:2202.13490*, 2022.
- [28] A. Bora, A. Jalal, E. Price, and A. G. Dimakis. Compressed sensing using generative models. In *International Conference on Machine Learning*, pages 537–546. PMLR, 2017.
- [29] C. A. Bouman. *Foundations of Computational Imaging: A Model-Based Approach*. SIAM, Philadelphia, PA, 2022.
- [30] A. Bourrier, M. E. Davies, T. Peleg, P. Pérez, and R. Gribonval. Fundamental performance limits for ideal decoders in high-dimensional linear inverse problems. *IEEE Transactions on Information Theory*, 60(12):7928–7946, 2014.
- [31] G. T. Buzzard, S. H. Chan, S. Sreehari, and C. A. Bouman. Plug-and-play unplugged: Optimization-free reconstruction using consensus equilibrium. *SIAM J. Imaging Sci.*, 11(3):2001–2020, 2018.
- [32] E. J. Candès, J. Romberg, and T. Tao. Robust uncertainty principles: exact signal reconstruction from highly incomplete frequency information. *IEEE Trans. Inform. Theory*, 52(2):489–509, 2006.
- [33] N. Carlini, P. Mishra, T. Vaidya, Y. Zhang, M. Sherr, C. Shields, D. Wagner, and W. Zhou. Hidden voice commands. In *25th USENIX Security Symp.*, pages 513–530, 2016.
- [34] N. Carlini and D. Wagner. Audio adversarial examples: Targeted attacks on speech-to-text. In *2018 IEEE Security and Privacy Worksh.*, pages 1–7, 2018.
- [35] W. Chen, D. Wipf, and M. Rodrigues. Deep learning for linear inverse problems using the plug-and-play priors framework. In *ICASSP 2021-2021 IEEE International Conference on Acoustics, Speech and Signal Processing (ICASSP)*, pages 8098–8102. IEEE, 2021.
- [36] K. Cheng, F. Calivá, R. Shah, M. Han, S. Majumdar, and V. Pedoia. Addressing the false negative problem of deep learning MRI reconstruction models by adversarial attacks and robust training. In T. Arbel, I. Ben Ayed, M. de Bruijne, M. Descoteaux, H. Lombaert, and C. Pal, editors, *Proceedings of the Third Conference on Medical Imaging with Deep Learning*, volume 121 of *Proceedings of Machine Learning Research*, pages 121–135. PMLR, 06–08 Jul 2020.
- [37] A. Cohen, W. Dahmen, and R. A. DeVore. Compressed sensing and best k -term approximation. *J. Amer. Math. Soc.*, 22(1):211–231, 2009.
- [38] R. Cohen, M. Elad, and P. Milanfar. Regularization by denoising via fixed-point projection (RED-PRO). *SIAM J. Imaging Sci.*, 14(3):1374–1406, 2021.
- [39] M. J. Colbrook, V. Antun, and A. C. Hansen. The difficulty of computing stable and accurate neural networks: On the barriers of deep learning and smale’s 18th problem. *Proc. Natl. Acad. Sci. USA*, 119(12):e2107151119, 2022.
- [40] N. Dang, M. Khurana, and S. Tiwari. MirGAN: medical image reconstruction using generative adversarial networks. In *2020 5th International Conference on Computing, Communication and Security (ICCCS)*, pages 1–5, 2020.
- [41] M. Z. Darestani, A. S. Chaudhari, and R. Heckel. Measuring robustness in deep learning based compressive sensing. In *International Conference on Machine Learning*, pages 2433–2444. PMLR, 2021.
- [42] A. D. Desai, A. M. Schmidt, E. B. Rubin, C. M. Sandino, M. S. Black, V. Mazzoli, K. J. Stevens, R. Boutin, C. Ré, G. E. Gold, et al. SKM-TEA: a dataset for accelerated MRI reconstruction with dense image labels for quantitative clinical evaluation. *arXiv:2203.06823*, 2022.
- [43] R. A. DeVore, G. Petrova, and P. Wojtaszczyk. Data assimilation and sampling in Banach spaces. *Calcolo*, 54:963–1007, 2017.
- [44] M. Dhar, A. Grover, and S. Ermon. Modeling sparse deviations for compressed sensing using generative models. In J. Dy and A. Krause, editors, *Proceedings of the 35th International Conference on Machine Learning*, volume 80 of *Proceedings of Machine Learning Research*, pages 1214–1223. PMLR, 10–15 Jul 2018.
- [45] D. L. Donoho. Compressed sensing. *IEEE Trans. Inform. Theory*, 52(4):1289–1306, 2006.
- [46] M. Duff, N. D. Campbell, and M. J. Ehrhardt. Regularising inverse problems with generative machine learning models. *arXiv:2107.11191*, 2021.
- [47] C. L. Epstein. *Introduction to the mathematics of medical imaging*. SIAM, 2007.
- [48] European Commission. Europe fit for the digital age: Commission proposes new rules and actions for excellence and trust in artificial intelligence. Press release: https://ec.europa.eu/commission/presscorner/detail/en/IP_21_1682, 21. April 2021. Accessed: 2022-08-09.

- [49] D. Evangelista, J. Nagy, E. Morotti, and E. L. Piccolomini. To be or not to be stable, that is the question: Understanding neural networks for inverse problems. *arXiv:2211.13692*, 2022.
- [50] K. Eykholt, I. Evtimov, E. Fernandes, B. Li, A. Rahmati, C. Xiao, A. Prakash, T. Kohno, and D. Song. Robust physical-world attacks on deep learning visual classification. In *IEEE Conference on Computer Vision and Pattern Recognition*, pages 1625–1634, 2018.
- [51] Q. Fan, T. Witzel, A. Nummenmaa, K. R. Van Dijk, J. D. Van Horn, M. K. Drews, L. H. Somerville, M. A. Sheridan, R. M. Santillana, J. Snyder, et al. MGH-USC human connectome project datasets with ultra-high b-value diffusion MRI. *Neuroimage*, 124:1108–1114, 2016.
- [52] A. Fawzi, S.-M. Moosavi-Dezfooli, and P. Frossard. The robustness of deep networks: A geometrical perspective. *IEEE Sign. Proc. Mag.*, 34(6):50–62, 2017.
- [53] S. G. Finlayson, J. D. Bowers, J. Ito, J. L. Zittrain, A. L. Beam, and I. S. Kohane. Adversarial attacks on medical machine learning. *Science*, 363(6433):1287–1289, 2019.
- [54] S. Foucart, C. Liao, S. Shahrampour, and Y. Wang. Learning from non-random data in Hilbert spaces: an optimal recovery perspective. *Sampl. Theory Signal Process. Data Anal.*, 20:5, 2022.
- [55] M. Gao, J. A. Fessler, and H.-P. Chan. Deep convolutional neural network with adversarial training for denoising digital breast tomosynthesis images. *IEEE Trans. Med. Imaging*, 40(7):1805–1816, 2021.
- [56] GE Healthcare. A bold new world: GE healthcare’s pioneering deep learning image reconstruction technology benefits more than 2 million patients globally. Press release: <https://www.ge.com/news/press-releases/a-bold-new-world-ge-healthcares-pioneering-deep-learning-image-reconstruction>, 6. May 2022. Accessed: 2022-09-22.
- [57] M. Geist, P. Petersen, M. Raslan, R. Schneider, and G. Kutyniok. Numerical solution of the parametric diffusion equation by deep neural networks. *J. Sci. Comput.*, 88:22, 2021.
- [58] M. Genzel, I. Gühring, J. Macdonald, and M. März. Near-exact recovery for tomographic inverse problems via deep learning. In K. Chaudhuri, S. Jegelka, L. Song, C. Szepesvari, G. Niu, and S. Sabato, editors, *Proceedings of the 39th International Conference on Machine Learning*, volume 162 of *Proceedings of Machine Learning Research*, pages 7368–7381. PMLR, 17–23 Jul 2022.
- [59] M. Genzel, J. Macdonald, and M. März. Solving inverse problems with deep neural networks – robustness included? *IEEE Trans. Pattern Anal. Machine Intellig.*, 2022.
- [60] D. Gilton, G. Ongie, and R. Willett. Model adaptation for inverse problems in imaging. *IEEE Trans. Comput. Imaging*, 7:661–674, 2021.
- [61] I. Goodfellow, J. Pouget-Abadie, M. Mirza, B. Xu, D. Warde-Farley, S. Ozair, A. Courville, and Y. Bengio. Generative adversarial nets. *Advances in neural information processing systems*, 27, 2014.
- [62] A. Gossard and P. Weiss. Training adaptive reconstruction networks for inverse problems. *arXiv:2202.11342*, 2022.
- [63] K. Gregor and Y. LeCun. Learning fast approximations of sparse coding. In *Proceedings of the 27th international conference on international conference on machine learning*, pages 399–406, 2010.
- [64] H. Gu, B. Yaman, S. Moeller, J. Ellermann, K. Ugurbil, and M. Akçakaya. Revisiting ℓ_1 -wavelet compressed-sensing MRI in the era of deep learning. *Proc. Natl. Acad. Sci.*, 119(33):e2201062119, 2022.
- [65] K. Hammernik, T. Klatzer, E. Kobler, M. P. Recht, D. K. Sodickson, T. Pock, and F. Knoll. Learning a variational network for reconstruction of accelerated MRI data. *Magnetic resonance in medicine*, 79(6):3055–3071, 2018.
- [66] N. P. Hardy, P. Mac Aonghusa, P. M. Neary, and R. A. Cahill. Intraprocedural artificial intelligence for colorectal cancer detection and characterisation in endoscopy and laparoscopy. *Surgical Innovation*, 28(6):768–775, 2021.
- [67] D. Heaven et al. Why deep-learning AIs are so easy to fool. *Nature*, 574(7777):163–166, 2019.
- [68] R. Heckel and P. Hand. Deep decoder: Concise image representations from untrained non-convolutional networks. In *International Conference on Learning Representations*, 2019.
- [69] R. Heckel and M. Soltanolkotabi. Compressive sensing with un-trained neural networks: Gradient descent finds a smooth approximation. In H. D. III and A. Singh, editors, *Proceedings of the 37th International Conference on Machine Learning*, volume 119 of *Proceedings of Machine Learning Research*, pages 4149–4158. PMLR, 13–18 Jul 2020.
- [70] E. H. Herskovits. Artificial intelligence in molecular imaging. *Annals of Translational Medicine*, 9(9), 2021.
- [71] D. P. Hoffman, I. Slavitt, and C. A. Fitzpatrick. The promise and peril of deep learning in microscopy. *Nature Methods*, 18(2):131–132, 2021.
- [72] Y. Huang, T. Würfl, K. Breininger, L. Liu, G. Lauritsch, and A. Maier. Some investigations on robustness of deep learning in limited angle tomography. In *International Conference on Medical Image Computing and Computer-Assisted Intervention*, pages 145–153. Springer, 2018.
- [73] A. Jalal, L. Liu, A. G. Dimakis, and C. Caramanis. Robust compressed sensing using generative models. In H. Larochelle, M. Ranzato, R. Hadsell, M. Balcan, and H. Lin, editors, *Advances in Neural Information Processing Systems*, volume 33, pages 713–727. Curran Associates, Inc., 2020.

- [74] K. H. Jin, M. T. McCann, E. Froustey, and M. Unser. Deep convolutional neural network for inverse problems in imaging. *IEEE Trans. Image Process.*, 26(9):4509–4522, 2017.
- [75] P. M. Johnson, G. Jeong, K. Hammernik, J. Schlemper, C. Qin, J. Duan, D. Rueckert, J. Lee, N. Pezzotti, E. D. Weerdt, et al. Evaluation of the robustness of learned MR image reconstruction to systematic deviations between training and test data for the models from the fastMRI challenge. In *International Workshop on Machine Learning for Medical Image Reconstruction*, pages 25–34. Springer, 2021.
- [76] Y. Jun, H. Shin, T. Eo, and D. Hwang. Joint deep model-based MR image and coil sensitivity reconstruction network (Joint-ICNet) for fast MRI. In *Proceedings of the IEEE/CVF Conference on Computer Vision and Pattern Recognition (CVPR)*, pages 5270–5279, June 2021.
- [77] D. Karkaloulos, S. Noteboom, H. E. Hulst, F. M. Vos, and M. W. Caan. Assessment of data consistency through cascades of independently Recurrent Inference Machines for fast and robust accelerated MRI reconstruction. *Physics in Medicine & Biology*, 2022.
- [78] F. Knoll, K. Hammernik, C. Zhang, S. Moeller, T. Pock, D. K. Sodickson, and M. Akcakaya. Deep-learning methods for parallel magnetic resonance imaging reconstruction: A survey of the current approaches, trends, and issues. *IEEE Signal Process. Mag.*, 37(1):128–140, 2020.
- [79] F. Knoll, T. Murrell, A. Sriram, N. Yakubova, J. Zbontar, M. Rabbat, A. Defazio, M. J. Muckley, D. K. Sodickson, C. L. Zitnick, et al. Advancing machine learning for MR image reconstruction with an open competition: Overview of the 2019 fastMRI challenge. *Magnetic resonance in medicine*, (84(6)):3054–3070, 2020.
- [80] P. Kuchment. *The Radon transform and medical imaging*. SIAM, 2013.
- [81] A. Kurakin, I. Goodfellow, and S. Bengio. Adversarial examples in the physical world. In *International Conference on Learning Representations*, 2017.
- [82] A. Lahiri. *Learning-based Algorithms for Inverse Problems in MR Image Reconstruction and Quantitative Perfusion Imaging*. PhD thesis, University of Michigan, 2021.
- [83] R. F. Laine, I. Arganda-Carreras, R. Henriques, and G. Jacquemet. Avoiding a replication crisis in deep-learning-based bioimage analysis. *Nature methods*, 18(10):1136–1144, 2021.
- [84] D. B. Larson, H. Harvey, D. L. Rubin, N. Irani, R. T. Justin, and C. P. Langlotz. Regulatory frameworks for development and evaluation of artificial intelligence-based diagnostic imaging algorithms: summary and recommendations. *Journal of the American College of Radiology*, 18(3):413–424, 2021.
- [85] M.-H. Laves, M. Tölle, and T. Ortmaier. Uncertainty estimation in medical image denoising with bayesian deep image prior. In *Uncertainty for Safe Utilization of Machine Learning in Medical Imaging, and Graphs in Biomedical Image Analysis*, pages 81–96. Springer, 2020.
- [86] J. Leuschner, M. Schmidt, P. S. Ganguly, V. Andriashen, S. B. Coban, A. Denker, D. Bauer, A. Hadjifaradji, K. J. Batenburg, P. Maass, and M. van Eijnatten. Quantitative comparison of deep learning-based image reconstruction methods for low-dose and sparse-angle CT applications. *Journal of Imaging*, 7(3), 2021.
- [87] b. liang, h. li, m. su, p. bian, x. li, and w. shi. Deep text classification can be fooled. In *the 27th int. joint conf. on artificial intelligence*, 2017.
- [88] D. Liang, J. Cheng, Z. Ke, and L. Ying. Deep magnetic resonance image reconstruction: Inverse problems meet neural networks. *IEEE Signal Process. Mag.*, 37(1):141–151, 2020.
- [89] Z.-P. Liang and P. C. Lauterbur. *Principles of magnetic resonance imaging*. SPIE Optical Engineering Press Bellingham, 2000.
- [90] J. Liu, S. Asif, B. Wohlberg, and U. Kamilov. Recovery analysis for plug-and-play priors using the restricted eigenvalue condition. *Advances in Neural Information Processing Systems*, 34:5921–5933, 2021.
- [91] X. Liu, B. Glocker, M. M. McCradden, M. Ghassemi, A. K. Denniston, and L. Oakden-Rayner. The medical algorithmic audit. *The Lancet Digital Health*, 2022.
- [92] K. Lønning, P. Putzky, J.-J. Sonke, L. Reneman, M. W. Caan, and M. Welling. Recurrent inference machines for reconstructing heterogeneous MRI data. *Medical image analysis*, 53:64–78, 2019.
- [93] A. Lucas, M. Iliadis, R. Molina, and A. K. Katsaggelos. Using deep neural networks for inverse problems in imaging: Beyond analytical methods. *IEEE Signal Process. Mag.*, 35(1):20–36, Jan 2018.
- [94] S. Lunz, O. Öktem, and C.-B. Schönlieb. Adversarial regularizers in inverse problems. *Advances in neural information processing systems*, 31, 2018.
- [95] M. Mardani, E. Gong, J. Y. Cheng, S. S. Vasanawala, G. Zaharchuk, L. Xing, and J. M. Pauly. Deep generative adversarial neural networks for compressive sensing MRI. *IEEE Trans. Med. Imaging*, 38(1):167–179, 2019.
- [96] M. Mardani, Q. Sun, D. Donoho, V. Pappas, H. Monajemi, S. Vasanawala, and J. Pauly. Neural proximal gradient descent for compressive imaging. In S. Bengio, H. Wallach, H. Larochelle, K. Grauman, N. Cesa-Bianchi, and R. Garnett, editors, *Advances in Neural Information Processing Systems*, volume 31. Curran Associates, Inc., 2018.
- [97] M. T. McCann, K. H. Jin, and M. Unser. Convolutional neural networks for inverse problems in imaging: A review. *IEEE Signal Process. Mag.*, 34(6):85–95, 11 2017.

- [98] M. T. McCann and M. Unser. Biomedical image reconstruction: From the foundations to deep neural networks. *Foundations and Trends® in Signal Processing*, 13(3):283–359, 2019.
- [99] D. W. McRobbie, E. A. Moore, M. J. Graves, and M. R. Prince. *MRI from Picture to Proton*. Cambridge University Press, 2 edition, 2006.
- [100] T. Meinhardt, M. Moller, C. Hazirbas, and D. Cremers. Learning proximal operators: Using denoising networks for regularizing inverse imaging problems. In *Proceedings of the IEEE International Conference on Computer Vision*, pages 1781–1790, 2017.
- [101] C. A. Micchelli and T. J. Rivlin. *A survey of optimal recovery*, volume Optimal Estimation in Approximation Theory of *The IBM Research Symposia Series*. Springer, Boston, MA, 1977.
- [102] V. Monga, Y. Li, and Y. C. Eldar. Algorithm unrolling: interpretable, efficient deep learning for signal and image processing. *IEEE Signal Process. Mag.*, 38(2):18–44, 2021.
- [103] J. N. Morshuis, S. Gatidis, M. Hein, and C. F. Baumgartner. Adversarial robustness of MR image reconstruction under realistic perturbations. In *International Workshop on Machine Learning for Medical Image Reconstruction*, pages 24–33. Springer, 2022.
- [104] M. J. Muckley, B. Riemenschneider, A. Radmanesh, S. Kim, G. Jeong, J. Ko, Y. Jun, H. Shin, D. Hwang, M. Mostapha, et al. Results of the 2020 fastMRI challenge for machine learning MR image reconstruction. *IEEE Trans. Med. Imaging*, 2021.
- [105] S. Mukherjee. A.I. versus M.D. – What happens when diagnosis is automated? *The New Yorker*, 4 2017.
- [106] F. Natterer and F. Wübbeling. *Mathematical methods in image reconstruction*. SIAM, 2001.
- [107] M. Neyra-Nesterenko and B. Adcock. Stable, accurate and efficient deep neural networks for inverse problems with analysis-sparse models. *arXiv:2203.00804*, 2022.
- [108] L. Oala, C. Heiß, J. Macdonald, M. März, G. Kutyniok, and W. Samek. Detecting failure modes in image reconstructions with interval neural network uncertainty. *International Journal of Computer Assisted Radiology and Surgery*, 16(12):2089–2097, 2021.
- [109] D. Obmann, J. Schwab, and M. Haltmeier. Deep synthesis network for regularizing inverse problems. *Inverse Problems*, 37(1):015005, 2020.
- [110] G. Ongie, A. Jalal, C. A. Metzler, R. G. Baraniuk, A. G. Dimakis, and R. Willett. Deep learning techniques for inverse problems in imaging. *IEEE J. Sel. Area. Inform. Theory*, 1(1):39–56, 2020.
- [111] G. Ortiz-Jiménez, A. Modas, S.-M. Moosavi-Dezfooli, and P. Frossard. Optimism in the face of adversity: Understanding and improving deep learning through adversarial robustness. *Proc. IEEE*, 109(5):635–659, 2021.
- [112] A. Pal and Y. Rathi. A review and experimental evaluation of deep learning methods for MRI reconstruction. *Machine Learning for Biomedical Imaging*, 1, 2022.
- [113] Philips. Philips MR SmartSpeed: Increased speed and image quality: Driven by speed and artificial intelligence. Webpage: <https://www.usa.philips.com/healthcare/resources/landing/smartspeed>, 2022. Accessed: 2022-09-22.
- [114] A. Pinkus. Approximation theory of the MLP model in neural networks. *Acta Numer.*, 8:143–195, 1999.
- [115] P. Putzky and M. Welling. Recurrent inference machines for solving inverse problems. *arXiv:1706.04008*, 2017.
- [116] C. Qiao, D. Li, Y. Guo, C. Liu, T. Jiang, Q. Dai, and D. Li. Evaluation and development of deep neural networks for image super-resolution in optical microscopy. *Nature Methods*, 18(2):194–202, 2021.
- [117] M. Raissi, P. Perdikaris, and G. E. Karniadakis. Physics-informed neural networks: a deep learning framework for solving forward and inverse problems involving nonlinear partial differential equations. *J. Comput. Phys.*, 378:686–707, 2019.
- [118] A. Raj, Y. Bresler, and B. Li. Improving robustness of deep-learning-based image reconstruction. In H. D. III and A. Singh, editors, *Proceedings of the 37th International Conference on Machine Learning*, volume 119 of *Proceedings of Machine Learning Research*, pages 7932–7942. PMLR, 13–18 Jul 2020.
- [119] Z. Ramzi, P. Ciuciu, and J.-L. Starck. XPDNet for MRI reconstruction: An application to the 2020 fastMRI challenge. *arXiv:2010.07290*, 2020.
- [120] Z. Ramzi, J. Starck, and P. Ciuciu. XPDNet for MRI reconstruction: An application to the 2020 fastMRI challenge. In *2021 ISMRM annual meeting, no. Abstract*, volume 275, 2021.
- [121] S. Ravishanker, J. C. Ye, and J. A. Fessler. Image reconstruction: From sparsity to data-adaptive methods and machine learning. *Proc. IEEE*, 108(1):86–109, 2020.
- [122] A. J. Reader, G. Corda, A. Mehranian, C. d. Costa-Luis, S. Ellis, and J. A. Schnabel. Deep learning for PET image reconstruction. *IEEE Trans. Radi. Plasma Med. Sci.*, 5(1):1–25, 2021.
- [123] B. Recht, R. Roelofs, L. Schmidt, and V. Shankar. Do ImageNet classifiers generalize to ImageNet? In K. Chaudhuri and R. Salakhutdinov, editors, *Proceedings of the 36th International Conference on Machine Learning*, volume 97 of *Proceedings of Machine Learning Research*, pages 5389–5400. PMLR, 09–15 Jun 2019.

- [124] Y. Romano, M. Elad, and P. Milanfar. The little engine that could: Regularization by denoising (RED). *SIAM J. Imaging Sci.*, 10(4):1804–1844, 2017.
- [125] S. H. Rudy, S. L. Brunton, J. L. Proctor, and J. N. Kutz. Data-driven discovery of partial differential equations. *Sci. Adv.*, 3(4), 2017.
- [126] C. M. Sandino, J. Y. Cheng, F. Chen, M. Mardani, J. M. Pauly, and S. S. Vasanawala. Compressed sensing: From research to clinical practice with deep neural networks: Shortening scan times for magnetic resonance imaging. *IEEE Signal Process. Mag.*, 37(1):117–127, Jan 2020.
- [127] J. Scarlett, R. Heckel, M. R. Rodrigues, P. Hand, and Y. C. Eldar. Theoretical perspectives on deep learning methods in inverse problems. *arXiv:2206.14373*, 2022.
- [128] J. Schlemper, J. Caballero, J. V. Hajnal, A. Price, and D. Rueckert. A deep cascade of convolutional neural networks for MR image reconstruction. In *Int. Conf. Inf. Proc. Med. Imaging*, pages 647–658. Springer, 2017.
- [129] C. Schwab and J. Zech. Deep learning in high dimension: neural network expression rates for generalized polynomial chaos expansions in UQ. *Anal. Appl. (Singap.)*, 17(1):19–55, 2019.
- [130] V. Shah and C. Hegde. Solving linear inverse problems using GAN priors: An algorithm with provable guarantees. In *2018 IEEE international conference on acoustics, speech and signal processing (ICASSP)*, pages 4609–4613. IEEE, 2018.
- [131] S. Shalev-Shwartz and S. Ben-David. *Understanding Machine Learning - From Theory to Algorithms*. Cambridge University Press, 2014.
- [132] L. Shen, J. Pauly, and L. Xing. NeRP: Implicit neural representation learning with prior embedding for sparsely sampled image reconstruction. *IEEE Trans. Neur. Net. Lear.*, pages 1–13, 2022.
- [133] E. Shimron, J. I. Tamir, K. Wang, and M. Lustig. Implicit data crimes: Machine learning bias arising from misuse of public data. *Proc. Natl. Acad. Sci.*, 119(13):e2117203119, 2022.
- [134] E. Y. Sidky, I. Lorente, J. G. Brankov, and X. Pan. Do CNNs solve the CT inverse problem? *IEEE Trans. Biomed. Eng.*, 68(6):1799–1810, 2020.
- [135] E. Y. Sidky and X. Pan. Report on the AAPM deep-learning sparse-view CT grand challenge. *Medical Physics*, 2022.
- [136] R. Singh, W. Wu, G. Wang, and M. K. Kalra. Artificial intelligence in image reconstruction: The change is here. *Physica Medica*, 79:113–125, 2020.
- [137] A. Sriram, J. Zbontar, T. Murrell, A. Defazio, C. L. Zitnick, N. Yakubova, F. Knoll, and P. Johnson. End-to-end variational networks for accelerated MRI reconstruction. In *International Conference on Medical Image Computing and Computer-Assisted Intervention*, pages 64–73. Springer, 2020.
- [138] R. Strack. Imaging: AI transforms image reconstruction. *Nature Methods*, 15(5):309, 2018.
- [139] C. Szegedy, W. Zaremba, I. Sutskever, J. Bruna, D. Erhan, I. J. Goodfellow, and R. Fergus. Intriguing properties of neural networks. In *Proceedings of the International Conference on Learning Representations*, 2014.
- [140] A. N. Tikhonov. On the stability of inverse problems. *Proceedings of the USSR Academy of Sciences*, 39:195–198, 1943.
- [141] M. Tölle, M.-H. Laves, and A. Schlaefter. A mean-field variational inference approach to deep image prior for inverse problems in medical imaging. In M. Heinrich, Q. Dou, M. de Bruijne, J. Lellmann, A. Schläfer, and F. Ernst, editors, *Proceedings of the Fourth Conference on Medical Imaging with Deep Learning*, volume 143 of *Proceedings of Machine Learning Research*, pages 745–760. PMLR, 07–09 Jul 2021.
- [142] M. Torres-Velázquez, W.-J. Chen, X. Li, and A. B. McMillan. Application and construction of deep learning networks in medical imaging. *IEEE Trans. Radi. Plasma Med. Sci.*, 5(2):137–159, 2020.
- [143] Y. Traonmilin and R. Gribonval. Stable recovery of low-dimensional cones in Hilbert spaces: One RIP to rule them all. *Applied and Computational Harmonic Analysis*, 45(1):170–205, 2018.
- [144] Y. Traonmilin, R. Gribonval, and S. Vaiter. A theory of optimal convex regularization for low-dimensional recovery. *arXiv:2112.03540*, 2021.
- [145] D. Ulyanov, A. Vedaldi, and V. Lempitsky. Deep image prior. In *Proceedings of the IEEE Conference on Computer Vision and Pattern Recognition (CVPR)*, June 2018.
- [146] G. Varoquaux and V. Cheplygina. Machine learning for medical imaging: methodological failures and recommendations for the future. *NPJ digital medicine*, 5(1):1–8, 2022.
- [147] S. V. Venkatakrisnan, C. A. Bouman, and B. Wohlberg. Plug-and-play priors for model based reconstruction. In *2013 IEEE Global Conference on Signal and Information Processing*, pages 945–948, 2013.
- [148] G. Wang, J. C. Ye, and B. De Man. Deep learning for tomographic image reconstruction. *Nature Machine Intelligence*, 2(12):737–748, 2020.
- [149] G. Wang, J. C. Ye, K. Mueller, and J. A. Fessler. Image reconstruction is a new frontier of machine learning. *IEEE Trans. Med. Imaging*, 37(6):1289–1296, 2018.
- [150] E. Weinan and B. Yu. The Deep Ritz Method: A Deep Learning-Based Numerical Algorithm for Solving Variational Problems. *Commun. Math. Stat.*, 6(1):1–14, 2018.

- [151] J. Whang, Q. Lei, and A. Dimakis. Compressed sensing with invertible generative models and dependent noise. In *NeurIPS 2020 Workshop on Deep Learning and Inverse Problems*, 2020.
- [152] D. H. Wolpert. The lack of a priori distinctions between learning algorithms. *Neural Comput.*, 8(7):1341–1390, 1996.
- [153] D. H. Wolpert and W. G. Macready. No free lunch theorems for optimization. *IEEE Trans. Evol. Comput.*, 1(1):67–82, 1997.
- [154] E. Wu, K. Wu, R. Daneshjou, D. Ouyang, D. E. Ho, and J. Zou. How medical AI devices are evaluated: limitations and recommendations from an analysis of FDA approvals. *Nature Medicine*, 27(4):582–584, 2021.
- [155] G. Yang, S. Yu, H. Dong, G. Slabaugh, P. L. Dragotti, X. Ye, F. Liu, S. Arridge, J. Keegan, Y. Guo, et al. DAGAN: Deep de-aliasing generative adversarial networks for fast compressed sensing MRI reconstruction. *IEEE Trans. Med. Imaging*, 2017.
- [156] y. yang, J. Sun, H. Li, and Z. Xu. Deep ADMM-Net for compressive sensing MRI. In D. Lee, M. Sugiyama, U. Luxburg, I. Guyon, and R. Garnett, editors, *Advances in Neural Information Processing Systems*, volume 29. Curran Associates, Inc., 2016.
- [157] T. Yu, T. Hilbert, G. F. Piredda, A. Joseph, G. Bonanno, S. Zenkhri, P. Omoumi, M. B. Cuadra, E. J. Canales-Rodríguez, T. Kober, et al. Validation and generalizability of self-supervised image reconstruction methods for undersampled MRI. *arXiv:2201.12535*, 2022.
- [158] C. Zhang, J. Jia, B. Yaman, S. Moeller, S. Liu, M. Hong, and M. Akçakaya. Instabilities in conventional multi-coil MRI reconstruction with small adversarial perturbations. In *2021 55th Asilomar Conference on Signals, Systems, and Computers*, pages 895–899. IEEE, 2021.
- [159] R. Zhao, B. Yaman, Y. Zhang, R. Stewart, A. Dixon, F. Knoll, Z. Huang, Y. W. Lui, M. S. Hansen, and M. P. Lungren. fastMRI+, clinical pathology annotations for knee and brain fully sampled magnetic resonance imaging data. *Scientific Data*, 9(1):1–6, 2022.
- [160] R. Zhao, Y. Zhang, B. Yaman, M. P. Lungren, and M. S. Hansen. End-to-end AI-based MRI reconstruction and lesion detection pipeline for evaluation of deep learning image reconstruction. *arXiv:2109.11524*, 2021.
- [161] B. Zhu, J. Z. Liu, S. F. Cauley, B. R. Rosen, and M. S. Rosen. Image reconstruction by domain-transform manifold learning. *Nature*, 555(7697):487, 03 2018.